


Article

Detrital-Zircon Geochronology of Jurassic–Cretaceous Strata in the Turpan-Hami Basin: Implication for the Late Mesozoic Tectonic Evolution of Eastern Tien Shan

Yang Qin ¹, Chiyang Liu ^{1,*}, Lihua Yang ¹, Heng Peng ^{1,2}  and Xiaoqin Jiao ²

¹ State Key Laboratory of Continental Dynamics, Department of Geology, Northwest University, Xi'an 710069, China; 202021427@stumail.nwu.edu.cn (Y.Q.); 201921119@stumail.nwu.edu.cn (L.Y.); pengheng@stumail.nwu.edu.cn (H.P.)

² Dipartimento di Geoscienze, Università di Padova, 35131 Padova, Italy; x.qinjiao@gmail.com

* Correspondence: lcy@nwu.edu.cn

Abstract: Detrital-zircon U-Pb geochronology is extensively used to imply provenance histories as one of the most common methods to constrain the tectonic evolution of ancient sedimentary systems. The rapid accumulation of detrital-zircon thermochronology data in the eastern Tien Shan region brought great convenience for understanding the basin–mountain evolution in the region. In this work, 41 samples for zircon U-Pb dating from the Jurassic–Cretaceous strata of the Turpan-Hami basin and its adjacent region were compiled. Based on the systematic investigation, comparison, and summarization of Late Mesozoic sources in the eastern Tien Shan region and the quantitative characterization of source variations, we further explored and dissected the Late Mesozoic tectonic evolution of the eastern Tien Shan orogenic belt. Data from detrital-zircon age spectra, KS tests, MDS plots, Monte Carlo simulations, etc., suggested that eastern Tien Shan was also highly active during the Mesozoic, and especially, Bogda was the most remarkable. Moreover, there was a significant differential segmental exhumation before the Late Jurassic. In general, from the Early Jurassic to the Cretaceous, the proportion of Bogda provenance gradually increased, especially the large-scale uplift and denudation that occurred after the development of the Qigu Formation. The provenance of central Tien Shan and Jueluotag gradually stabilized before the Cretaceous. From the Late Jurassic to the Cretaceous, the decreasing tendency of the central-Tien-Shan-provenance percentages decreased, while that of Jueluotag provenance increased. Furthermore, central Tien Shan provenance had a slightly growing trend from the Early Jurassic (38%) to the Middle Jurassic (41.3%) and then gradually decreased to 20.3%. The Central Tien Shan still accounted for a sizeable proportion of the provenance, the genesis of which suggests that it may be that provenance ascribable to central Tien Shan still crossed the poorly uplifted Jueluotag to the Turpan-Hami basin. Similar to central Tien Shan, the provenance ascribable to Jueluotag gradually decreased from an initial 51.8% to 14.9% in the Late Jurassic, but the proportion of the provenance increased again to 26% during the Cretaceous. These features opened the prelude to the Cenozoic tectonic activities in this region. In addition, the decomposition results revealed that the inverse Monte Carlo mixed model for dissecting the provenance of sandstone samples was subject to large biases in complex geological settings, such as detrital-zircon populations, the age spectra of source areas, contemporaneous magmatism, and recovered older strata.

Keywords: detrital-zircon U-Pb; Jurassic–Cretaceous; Bogda; Turpan-Hami basin; provenance; tectonic evolution



Citation: Qin, Y.; Liu, C.; Yang, L.; Peng, H.; Jiao, X. Detrital-Zircon Geochronology of Jurassic–Cretaceous Strata in the Turpan-Hami Basin: Implication for the Late Mesozoic Tectonic Evolution of Eastern Tien Shan. *Minerals* **2022**, *12*, 926. <https://doi.org/10.3390/min12080926>

Academic Editor: Simon Paul Johnson

Received: 25 May 2022

Accepted: 18 July 2022

Published: 22 July 2022

Publisher's Note: MDPI stays neutral with regard to jurisdictional claims in published maps and institutional affiliations.



Copyright: © 2022 by the authors. Licensee MDPI, Basel, Switzerland. This article is an open access article distributed under the terms and conditions of the Creative Commons Attribution (CC BY) license (<https://creativecommons.org/licenses/by/4.0/>).

1. Introduction

Detrital-zircon U-Pb dating is extensively used in tectonic geology, sedimentary geology, and geomorphology [1,2]. Because of their refractory nature, zircons survive most

erosion and weathering processes and remain chemically intact; thus, they provide a continuous record of sedimentary–tectonic evolution history where sedimentary-strata records fail [1]. The precise U-Pb analysis of sandstone allows the detrital-zircon ages to be matched to the crystallization ages of potential sources, which can be regarded as valuable indicators of potential provenance. Although the sources of detrital-zircon age groups are not unique and convergence may bring together different detrital-zircon assemblages from multiple separate primary and/or regenerated secondary sources, it is practical and necessary for the interpretation of sources, and it offers new opportunities for provenance studies and paleogeographic reconstructions [3–5]. With the development of high-precision methods for zircon age dating, such as laser-ablation-induced coupled-plasma mass spectrometry and sensitive high-resolution ion microprobing, the transition to more quantitative methods has gradually begun over the last 20 years, with a wide range of applications in the interpreting of provenance [6–8]. However, with the accumulation of large amounts of detrital-zircon data, convenience can be combined with trouble; this number of data presents challenges for its management, visualization, and interpretation [6], especially when there are inconsistencies among the data. In this case, we need to review these data in a holistic, integrated view. Noteworthy, the differences in the age frequency distributions of the samples are normally assessed qualitatively with visual comparisons, such as probability density plots (PDPs), cumulative-distribution functions (CDFs), CDF–cross plots, or kernel density estimates (KDEs); these are and could continue to be foundational for detrital-zircon data interpretation and research.

However, these visualization methods are becoming increasingly problematic due to the size of the sample population. Although large datasets are essential for continental-scale or high-resolution comparisons, the interpretation of these large datasets often relies on the visual comparisons of full-page or multi-page age-distribution plots. Early interpretation methods of detrital age distributions rely on a qualitative comparison based on the presence or absence of characteristic source populations for a given geologic setting. Visual inspection also prevents the quantitative comparisons of samples, hampering the application of forwarding mixed models and increasing the potential for subjectivity or approximation in interpretation. The increasing size of such datasets has resulted in a growing desire for a more robust characterization of differences. Methodologies have been successfully employed thus far, including quantifying the source mixing proportions (e.g., optimized forward modeling) [8,9] and the multidimensional scaling (MDS) approach [6].

Situated along the southern margin of the Central Asian Orogenic Belt (CAOB), Tien Shan is one of the largest Paleozoic accretionary orogens in the world (Figure 1a) [10–15]. The Tien Shan orogen underwent complex tectonic evolution from the Paleozoic [16–19]. It is generally accepted that the Paleozoic Tien Shan orogenic belt was reactivated during the Cenozoic [20–22]. However, recent studies suggested that the Tien Shan was also highly active during the Mesozoic [23–27]. Apparently, the interpretations of the activeness of the Tien Shan orogenic belt in the Mesozoic are controversial, especially for Bogda.

The Bogda belt, an essential branch of Tien Shan, separates the Junggar basin from the Turpan-Hami basin (Figure 1b). The Jurassic–Cretaceous basin-range systems between Bogda and its adjacent basins are crucial for our knowledge of the Mesozoic activeness of the Tien Shan orogenic belt [26,28]. Numerous studies revealed the Early Jurassic–Early Cretaceous exhumation history of the Bogda based on sedimentology, petrology, paleocurrent, heavy minerals, fission-track analyses, and detrital-zircon U-Pb dating [29–34], but no consensus was reached. According to the results from sedimentary phases, sediment composition, paleocurrents, regional unconformities, and statistical analyses, several researchers proposed an Early Jurassic uplift of Bogda [24,29–36]. However, regarding the sedimentary successions in the Badaowan Formation, data from detrital-zircon dating and heavy-mineral analyses indicated that Bogda did not experience any uplift during the Early Jurassic [25,37,38]. There is no doubt that there is no consensus on the onset time of the Bogda uplift. Moreover, in accordance with the reconstruction of the Permian–Jurassic source-sink system in the southern Junggar basin, Zhao et al. (2020) concluded that the

eastern Bogda did not experience an uplift after the Middle Jurassic. However, heavy-mineral and detrital-zircon dating suggested that eastern Bogda began to experience an uplift after the Late Jurassic [26] and that an intense uplift of Bogda occurred during the Late Jurassic–Early Cretaceous [39–44].

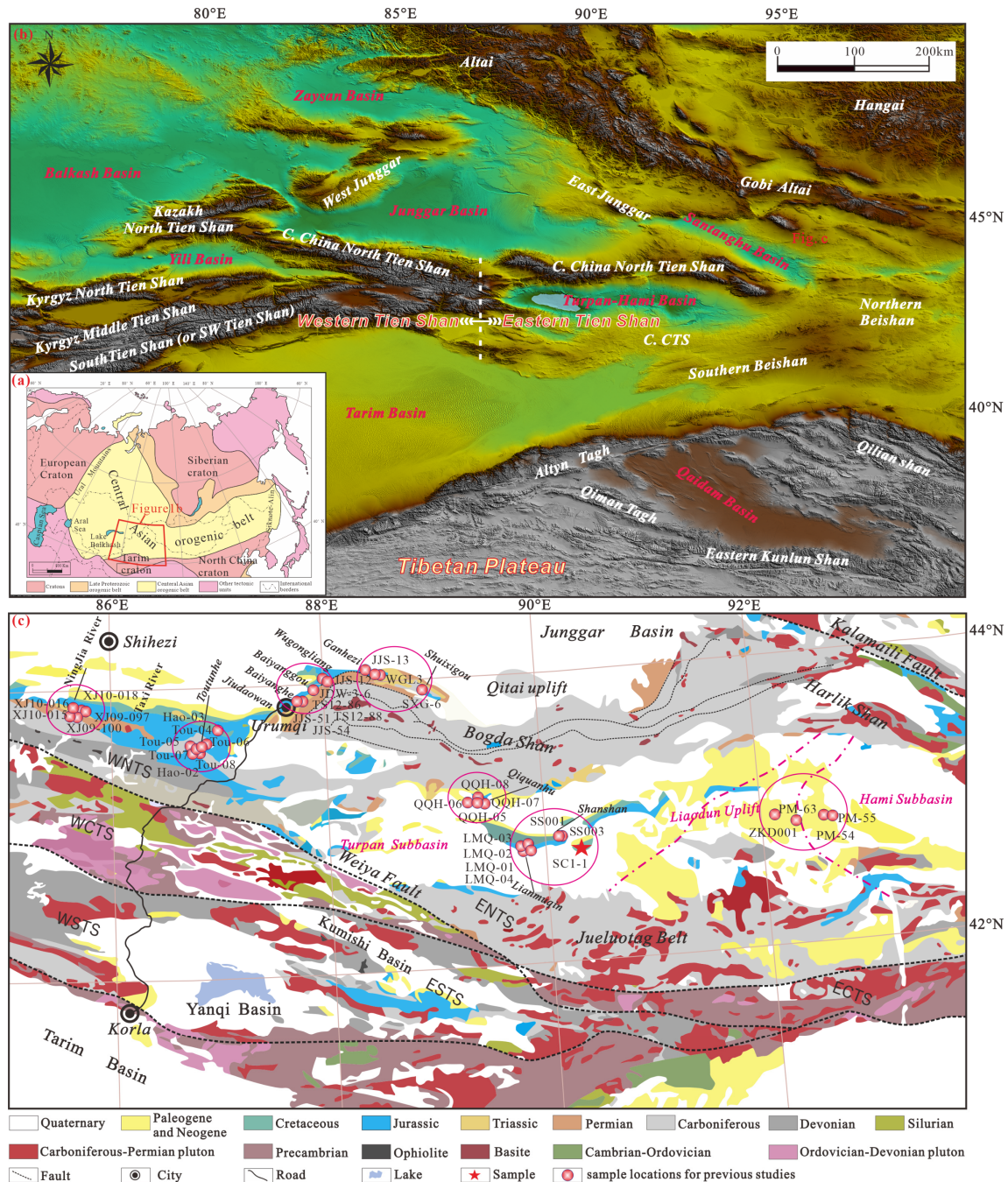


Figure 1. (a) Tectonic location of the Central Asian Orogenic Belt, modified from [33]; (b) digital topographical map of Tien Shan and its adjacent areas; (c) Geological map of eastern Tien Shan and location of detrital-zircon U-Pb-dating study samples, modified from [24]. Abbreviations: WNTS = Western–North Tien Shan; WCTS = Western–Central Tien Shan; WSTS = Western–South Tien Shan; ENT = Eastern–North Tien Shan; ECTS = Eastern–central Tien Shan; ESTS = Eastern–South Tien Shan.

Meanwhile, considerable work was finalized with respect to the tectonism that occurred in the Late Mesozoic in the eastern Tien Shan region, such that a significant number

of chronological data was duly accumulated. However, the contradiction remains among the time of the uplift deduced from thermochronology analyses, the times confined with sedimentological methods, and the times determined using heavy minerals. In addition, the spatial and temporal comparisons in the previous analyses of zircon data from the Bogda region are relatively weak, and the conclusions explored are influenced by the regional features of the study region to various degrees. For these reasons, it is necessary to conduct more detailed work and utilize more effective methods to comprehend the tectonic and provenance evolution of the Bogda region from the Early Jurassic to the Cretaceous.

In this work, we collected the Jurassic–Cretaceous detrital-zircon U–Pb results obtained from samples that came from the western section of northern Tien Shan, northwestern Bogda, southern Bogda, and the interior of the Tupan-Hami basin to constrain the sources of the Tupan-Hami-basin sediments in the context of the tectonic setting and the paleoclimatic and sedimentary facies of eastern Tien Shan at this time. Here, we characterized sample–sample and provenance–sample affinities and spatial–temporal provenance variations predominantly using statistics (KS tests), multidimensional scaling (MDS), and detrital-zircon mixed methods. Using these methods, we obtained and we here present a relatively comprehensive overview of the tectonic evolution of eastern Tien Shan and the provenance transition processes in the Tupan-Hami basin. At the same time, we examined the feasibility of the inverse Monte Carlo mixed model for dissecting sandstone samples’ provenance.

2. Geological Setting

2.1. Regional Geological Setting and Potential Sources

The Central Asian Orogenic Belt (CAOB), delimited by the European Craton to the west, the Siberian Craton to the east, and the Tarim Craton and the North China Craton to the south (Figure 1a) [11,12,45,46], is a large accretionary orogenic belt that records the subduction and closure of the Paleo-Asian Ocean [10–15]. Most researchers propose that the CAOB was formed during the Paleozoic by the multiple convergence and accretion of various oceanic and continental terranes (Figure 1a) [11,45,47–53]. The Tien Shan orogenic belt, as an essential component of the southwestern CAOB system [12,19,47,52–54], extends approximately 2500 km nearly east–west, reaching from northwest China to Kazakhstan, Kyrgyzstan, and Tajikistan [12,19,55]. The majestic landscapes of Tien Shan were mainly formed as a result of the Cenozoic Indian–Eurasian collision orogeny [36,56–58], inducing the renewed folding orogeny and rapid uplift of the Paleozoic orogenic belt formed by the closure of the Paleo-Asian Ocean [11,16,49,54,57].

The Chinese Tien Shan orogen, an essential component of the Tien Shan orogen, is situated in Northern China’s Xinjiang Uyghur Autonomous Region. It can be roughly divided into eastern and western geographical units along the Urumqi–Kurla transect in northern Xinjiang. Tectonically, the Tien Shan orogenic belt can be subdivided into the southern, central, and northern Tien Shan orogens (Figure 1b,c), which are bounded by suture zones and deep faults (Figure 1c) [59].

Northern Tien Shan refers to the region between the Kalamaili fault to the north and the Weiya fault to the south, which contains several tectonic belts around the Turpan-Hami basin, such as the Bogda and the Harlik belts to the north and the Jueluotag belt to the south [19,54]. The Bogda belt is situated between the Junggar and the Turpan-Hami basins and is dominated by Carboniferous strata, including Lower Carboniferous marine volcanic felsic tuffs, tuffaceous sandstones, and volcanic lava, and Upper Carboniferous shallow marine tuffs, and clastic deposits, with submarine basalt, andesite, rhyolite, and felsic tuffs [60–62]. The Permian–Mesozoic sedimentary strata are discontinuously distributed along the piedmont of the Bogda belt, consisting of Lower Permian terrestrial clastic sediments and bimodal volcanic lava, and Middle Permian–Mesozoic terrestrial clastic sediments [35,61,62], and no pre-Carboniferous strata are exposed [23,25,33,63]. In brief, intense Late Paleozoic magmatism occurred in Bogda, lasting from 345 to 278 Ma [64].

Jueluotag is further subdivided from south to north by the Yamansu and Kanggar faults in the Yamansu belt, the Kanggar shear zone, and the Dananhu belt [19,54,65]. The

Yamansu belt predominantly consists of Carboniferous volcanic rocks, including basalt, andesite, and minor rhyolite interbedded with clastic sediments [54,66]. Greenschists and ductile deformed Devonian–Carboniferous volcanic sedimentary rocks are mainly found in the southern part of the Kanggar shear zone, while ophiolitic fragments primarily dominate in the northern part [67,68]. The Dananhu belt mainly consists of Ordovician–Silurian marine clasts and tuffs with minor limestone and basalt; Devonian basaltic–feldspathic volcanic rocks and volcanic clastic rocks; Carboniferous basalt, basaltic andesite, and rhyolite, with minor sandstone and tuffs; and Permian intercalated basalt, andesite, and rhyolite clasts [54,69].

The Harlik belt is interpreted as an Ordovician–Late Carboniferous continental island arc that is ascribed to the southward subduction of the Karamay Ocean [54,70,71] or the northward subduction of the North Tien Shan Ocean [65]. The oldest stratum in the Harlik belt is the Late Ordovician–Early Silurian Huangcaopo Formation, mainly consisting of felsic volcanic rocks, marine metamorphic clastic rocks, volcanic clastic sedimentary rocks, volcanic clastic rocks, and accessory dacite [70,72]. Devonian strata consist of volcanic clastic rocks, arc-associated long-interstitial volcanic rocks, and marine clastic rocks [71,73]. The Harlik belt and the Dananhu belt have similar stratigraphic sequences and rock assemblages [54]. In summary, Paleozoic intrusive and eruptive magmatism ages of 460–260 Ma are widespread in Jueluotag [54,59,74].

Central Tien Shan mainly consists of Precambrian basement and Paleozoic volcanic sedimentary rocks and is thus regarded as a Precambrian micro-continent [75–77]. Precambrian basement rocks underwent upper-greenschist–amphibole-facies metamorphism accompanied with major magmatism values of ~2.5, ~1.8, and ~1.45–0.65 Ga [77], and Paleozoic strata are dominated by Cambrian–Carboniferous greenschist, slate, limestone, and volcanic–siliceous clastic rocks. Paleozoic plutons are widely exposed [78], with crystallization ages ranging from 500 to 250 Ma [74,78]. In addition, the reactivation of Early Mesozoic magmatic events (crystallization ages ~250–223 Ma) was detected in central and northern Tien Shan [65].

Southern Tien Shan, a broad suture zone formed by the closure of the South Tien Shan Ocean between central Tien Shan and the Tarim Craton, is characterized by well-preserved ophiolite [18,54,79]. The unit is dominated by low–medium-grade and unaltered sequences of Silurian–Carboniferous ages, as well as discontinuous ophiolite fragments, high-pressure metamorphic rocks, and sepiolite [19,54,79].

2.2. The Turpan-Hami Basin

The Turpan-Hami basin (Figure 1c), also referred to as the Tuha basin in China [29,42], an elongated intra-montane basin approximately 500 km long from east to west and nearly 100 km wide from north to south within northern Tien Shan, contains non-marine Meso-Cenozoic infill. It is situated on a substrate of Ordovician–Lower Carboniferous metamorphic sedimentary rocks and marine crustal fragments [80] and is enriched with a variety of mineral resources, such as oil, gas, coal, and uranium [34,81,82].

Predecessors have carried out numerous studies on the Turpan-Hami basin, but there are different schools of thought in terms of basin basement and evolution. Although most previous studies emphasize that the basin was formed in the Early Permian [83], some studies argue that it developed as an intra-land rift during the Carboniferous [84,85]. Early Permian magmatism in and around Bogda implies that the Turpan-Hami basin was formed in an extensional setting, with the existence of a larger Turpan–Junggar basin [86,87], later separated from the Junggar basin by the uplift of Bogda during the Jurassic [32,88]. The evolution of the Turpan-Hami basin from a Permian intra-land basin to a Cenozoic foreland basin may have been a consequence of the far-field effects of the Indian–Eurasian collision, and the Jurassic subsidence was caused by extensional tectonics [16,86,89]. The Turpan-Hami basin consists of the Turpan subbasin, the Liaodun uplift, and the Hami subbasin. The sedimentary sequences of the Turpan-Hami basin mainly developed in the Turpan and Hami subbasins, while the Liaodun uplift only partially deposited in the Lower and

Middle Jurassic [34,83]. Basin infill and subsequent cover, ranging from Carboniferous to Quaternary sediments, have an overall thickness of more than 9000 m [90,91].

The Jurassic–Cretaceous strata of the Turpan-Hami basin consist of the Lower Jurassic Badaowan and Sangonghe Formations; the Middle Jurassic Xishanyao, Sanjianfang, and Qiketai Formations; the Upper Jurassic Kalaza Formation; the Early Cretaceous Tugulu Group; and the Late Cretaceous Kumutake Formation. Those in the southern margin of the Junggar basin are composed of the Early Jurassic Badaowan and Sangonghe Formations, the Middle Jurassic Xishanyao and Toutunhe Formations, and the Upper Jurassic Qigu and Kalaza Formations, as well as the Early Cretaceous Tugulu Group and the Upper Cretaceous Kumutake Formation (Figure 2). Thick coal seams interbedded with coarse-grained clastic rocks characterize the Badaowan Formation; the Sangonghe Formation is typically composed of fine-grained clastic rocks and locally intercalated with non-marine limestones; the Xishanyao Formation consists of sandstones, siltstones, mudstones, and thick coal seams; the Sanjianfang Formation is mainly composed of red, sandy mudstones; the Qiketai Formation consists of yellowish-green sandstones and siltstones with bivalves; the Qigu Formation consists of purple, sandy mudstones with ostracods, and purple sandstones having intercalations of sandy mudstones dominate the Kalaza Formation [34,91]; the Tugulu Group is mainly composed of gray-black, gray-green, and purplish-red mudstones and is locally interbedded with gray siltstones; the Kumutake Formation is principally composed of thick-bedded gray fine sandstone.

| System | Series | southern Junggar Basin | Bogda | | Turpan-Hami Basin |
|------------|--------|----------------------------------|----------------------------------|-------------------------------------|-------------------------------------|
| | | | Northwestern | Southern | |
| Cretaceous | Upper | Donggou Fm.(K _{2d}) | | | Kumutake Fm.(K _{2k}) |
| | Lower | Tugulu Gp.(K _{1tg}) | | | Tugulu Gp.(K _{1tg}) |
| Jurassic | Upper | Kalaza Fm.(J _{3k}) | Kalaza Fm.(J _{3k}) | Kalaza Fm.(J _{3k}) | Kalaza Fm.(J _{3k}) |
| | | Qigu Fm.(J _{3q}) | Qigu Fm.(J _{3q}) | Qigu Fm.(J _{3q}) | Qigu Fm.(J _{3q}) |
| | Middle | Toutunhe Fm.(J _{2-3t}) | Toutunhe Fm.(J _{2-3t}) | Qiketai Fm.(J _{2-3q}) | Qiketai Fm.(J _{2-3q}) |
| | | | | Sanjianfang Fm.(J _{2-3s}) | Sanjianfang Fm.(J _{2-3s}) |
| | | Xishanyao Fm.(J _{2x}) | Xishanyao Fm.(J _{2x}) | Xishanyao Fm.(J _{2x}) | Xishanyao Fm.(J _{2x}) |
| | Lower | Sangonghe Fm.(J _{1s}) | Sangonghe Fm.(J _{1s}) | Sangonghe Fm.(J _{1s}) | Sangonghe Fm.(J _{1s}) |
| | | Badaowan Fm.(J _{1b}) | Badaowan Fm.(J _{1b}) | Badaowan Fm.(J _{1b}) | Badaowan Fm.(J _{1b}) |

Figure 2. Chronostratigraphic correlation diagram for the Jurassic–Cretaceous strata from the southern Junggar basin, Bogda, and Turpan-Hami basin.

3. Datasets and Analytical Methods

3.1. Datasets

In this study, we collected published detrital-zircon U-Pb data of the eastern Tien Shan region, including 8 Early Jurassic samples (7 from the Badaowan Formation and 1 from the Sangonghe Formation), 13 Middle Jurassic samples (6 from the Xishanyao Formation, 4 from the Toutunhe Formation, 1 from the Sanjianfang Formation, and 2 from the Qiketai Formation), 8 Late Jurassic samples (7 from the Qigu Formation and 1 from the Kalaza Formation), and 11 Cretaceous samples (9 from the Lower Cretaceous and 2 from the Upper Cretaceous) (Table 1). In this study, one Cretaceous Tugulu group sandstone sample (sample SC1-1) was collected from Well SC1 in the southern Turpan-Hami basin (Table 1). The position details of Well SC1 are shown in Figures 1c and 3.

Table 1. Summary of samples statistics (data from [23–26,33,35,43,63] and this study). See Figures 1c and 3 for details of the locations.

| Sample | Stratigraphic Unit | Formation | Latitude (N) | Longitude (W) | Type | Reference |
|----------|--------------------|-------------|--------------|---------------|------------|------------|
| LMQ-04 | K _{2k} | Kumutake | 42°50'23.41" | 89°52'37.14" | Outcrop | [24] |
| XJ10-015 | K _{2d} | Donggou | / | / | Outcrop | [63] |
| PM55-15 | K _{1d2} | Daihaidao | 42°43'34.29" | 92°30'39.24" | Outcrop | [43] |
| PM63-19 | K _{1d1} | Daihaidao | 42°44'02.75" | 92°35'49.65" | Outcrop | [43] |
| PM63-18 | K _{1d1} | Daihaidao | 42°44'02.75" | 92°35'49.65" | Outcrop | [43] |
| PM63-9 | K _{1d1} | Daihaidao | 42°44'02.75" | 92°35'49.65" | Outcrop | [43] |
| PM63-6 | K _{1d1} | Daihaidao | 42°44'02.75" | 92°35'49.65" | Outcrop | [43] |
| PM54-3 | K _{1l} | Liushuquan | 42°43'34.29" | 92°30'39.24" | Outcrop | [43] |
| XJ10-016 | K _{1tg} | Tugulu | / | / | Outcrop | [63] |
| SC1-1 | K _{1tg} | Tugulu | 42°52'56" | 90°32'7" | Drill hole | This study |
| Tou-08 | K _{1tg} | Tugulu | 43°47'51.12" | 87°16'39.9" | Outcrop | [24] |
| LMQ-03 | K _{1tg} | Tugulu | 42°49'56.63" | 89°52'06.60" | Outcrop | [24] |
| Tou-07 | J _{3k} | Kalaza | 43°47'0.84" | 87°12'8.28" | Outcrop | [23] |
| LMQ-02 | J _{3q} | Qigu | 42°49'49.24" | 89°51'28.20" | Outcrop | [24] |
| QQH-08 | J _{3q} | Qigu | 43°10'20.43" | 89°23'58.88" | Outcrop | [24] |
| Tou-06 | J _{3q} | Qigu | 43°47'0.84" | 87°15'49.38" | Outcrop | [23] |
| XJ09-100 | J _{3q} | Qigu | / | / | Outcrop | [63] |
| TS12-110 | J _{3q} | Qigu | / | / | Outcrop | [35] |
| ZKD001 | J _{3q} | Qigu | 42°40'35.05" | 92°24'03.44" | Drill hole | [43] |
| SS001 | J _{3q} | Qigu | 42°56'56.89" | 90°32'13.97" | Drill hole | [43] |
| LMQ-01 | J _{2-3q} | Qiketai | 42°49'46.98" | 89°51'25.76" | Outcrop | [24] |
| QQH-07 | J _{2-3q} | Qiketai | 43°10'18.12" | 89°23'52.75" | Outcrop | [24] |
| Tou-05 | J _{2-3t} | Toutunhe | 43°43'59.88" | 87°13'18.84" | Outcrop | [23] |
| XJ10-018 | J _{2t} | Toutunhe | / | / | Outcrop | [63] |
| SS003 | J _{2t} | Toutunhe | 42°57'45.73" | 90°32'22.31" | Outcrop | [43] |
| JJS-54 | J _{2t} | Toutunhe | 43°58'55.52" | 87°52'08.85" | Outcrop | [25] |
| QQH-06 | J _{2-3s} | Sanjianfang | 43°09'53.81" | 89°24'17.50" | Outcrop | [24] |
| JDW-6 | J _{2x} | Xishanyao | 43°54'40.09" | 87°40'38.47" | Outcrop | [26] |
| JDW-3 | J _{2x} | Xishanyao | 43°54'35.94" | 87°40'38.28" | Outcrop | [26] |
| TS12-88 | J _{2x} | Xishanyao | / | / | Outcrop | [35] |
| Tou-04 | J _{2x} | Xishanyao | 43°43'33.18" | 87°16'51.00" | Outcrop | [23] |
| WGL-03 | J _{2x} | Xishanyao | 44°04'02" | 88°12'11" | Outcrop | [26] |
| QQH-05 | J _{2x} | Xishanyao | 43°09'50.34" | 89°23'40.56" | Outcrop | [24] |
| Hao-03 | J _{1s} | Sangonghe | 43°40'58.86" | 87°12'8.28" | Outcrop | [23] |
| JJS-51 | J _{1b} | Badaowan | 43°57'16.62" | 87°54'16.29" | Outcrop | [25] |
| Hao-02 | J _{1b} | Badaowan | 43°39'21.9" | 87°13'2.04" | Outcrop | [23] |
| TS12-86 | J _{1b} | Badaowan | / | / | Outcrop | [35] |
| JJS-13 | J _{1b} | Badaowan | 43°57'23" | 87°56'10" | Outcrop | [25] |
| SXG-6 | J _{1b} | Badaowan | 43°55'51.34" | 89°01'33.82" | Outcrop | [25] |
| JJS-12 | J _{1b} | Badaowan | 44°04'33.00" | 88°24'03.74" | Outcrop | [25] |
| XJ09-097 | J _{1b} | Badaowan | / | / | Outcrop | [63] |

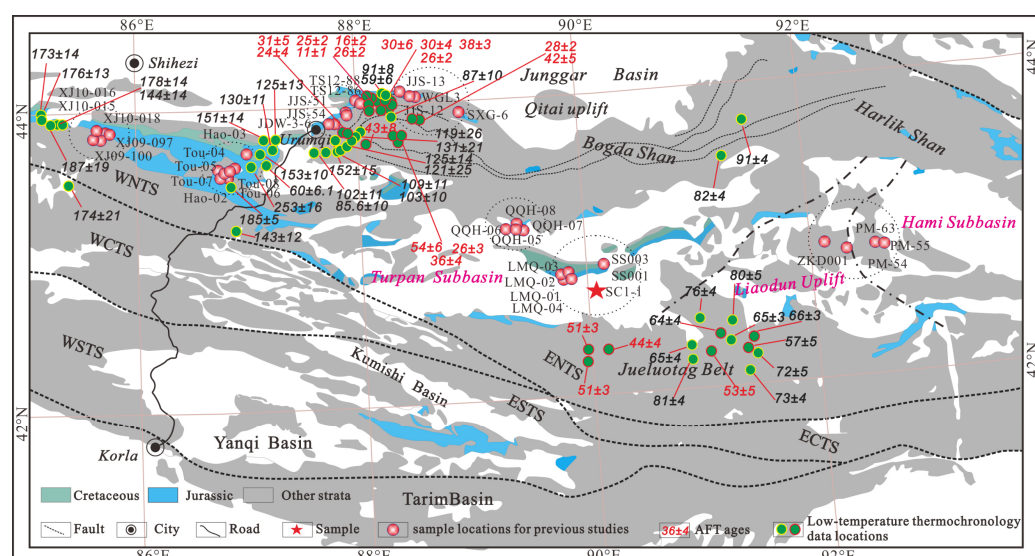


Figure 3. Geographic location of detrital-zircon samples and the apatite-fission-track age-distribution characteristics in the Turpan-Hami basin and its adjacent areas (the ages were obtained from [37,92–101] and references therein).

3.2. Analytical Methods

In this research study, to visually compare the differences in the age distributions of the contemporaneous detrital-zircon samples, the data were first plotted with the MATLAB-based stacked distribution plotter module in AgeCalcML-1.42, DZmds-1.10, to produce kernel density distribution (KDE) plots for each period time and conduct the multidimensional scaling (MDS) of all the samples [8]. MDS is used to calculate significant differences between pairs of samples to generate point plots, where the more similar two samples are to each other on the plot, the closer the distance is; conversely, the further away they are [6].

Subsequently, in attempting to quantify the similarity between the age distributions of detrital zircons, Kolmogorov–Smirnov (K-S) tests were performed on the detrital-zircon age data from various epochs using statistical methods [102]. KS testing is used to convert the detrital-zircon probability spectra into a cumulative-density arrangement and statistically compare the maximum difference between two cumulative-density functions. The underlying criterion for the KS test is the p -value; in general, when $p > 0.05$, the two samples are similar, and a confidence level of >95% exists; when p -value < 0.05 , the two samples are significantly different.

To derive a mixed proportion of source contributions, a recently released MATLAB-based inverse Monte Carlo method was also employed [8]. By constructing a random distribution of known source ages to compare them with the corresponding individual mixed-zircon-sample ages, this technique can be used to constrain the forward-optimization route to find the best-fitting model. We then determined the proportional contribution of the source area to each of the tested mixed samples. The quantitative comparison methods used in the mixed model (KS D, Kuiper V, and Cross-correlation) gave broadly similar results based on tests involving both synthetic and empirical data. Each method reproduced the proportion of the mixture of source age distributions from simple and complex synthetic data with a high degree of confidence. Sundell and Saylor's sensitivity tests on complex synthetic data indicated that the mixed model could sample the full range of source-sample weightings and yield sample age distributions as CDFs and PDPs with similar known distributions. A poor model fit was attributed to the inadequate characterization of the source and/or mixing samples. Given that samples SXG-6, JJS-12, and JJS-13 shared the same major age peaks, we merged their original data as one input to DZ-mix-1.21. Detailed information on the inverse Monte Carlo method is provided in Sundell and Saylor [7].

4. Results

This study analyzed one sandstone sample collected at well SC1 in the Turpan-Hami basin, with 108 zircon grains in total. Among the collected data, we obtained 107 detrital-zircon ages with concordances ranging from 90% to 110%. The zircon U-Pb concordia plots and representative cathodoluminescence images of the analyzed grains are presented. The isotopic information and ages obtained with all analyses are listed in Supplementary Materials Table S1. In addition, we processed and introduced the new and collected sample data to a uniform standard. The accepted ages were selected from a subset of both $\leq 10\%$ discordance and $\leq 10\%$ uncertainty (1σ), wherein the $^{206}\text{Pb}/^{238}\text{U}$ and $^{207}\text{Pb}/^{206}\text{Pb}$ ages were adopted for zircons younger and older than 1 Ga, respectively. Therefore, we removed discordant ages from our own data and those collected from references, and all data are listed in Supplementary Materials Table S2. The concordance was calculated as follows: $100 \times (^{206}\text{Pb}/^{207}\text{Pb} \text{ age}) / (^{206}\text{Pb}/^{238}\text{U} \text{ age})$ for ages older than 1 Ga, and $100 \times (^{207}\text{Pb}/^{235}\text{U} \text{ age}) / (^{206}\text{Pb}/^{238}\text{U} \text{ age})$ for ages younger than 1 Ga.

4.1. Zircon Morphology, Origin, and U-Pb Ages

The zircon grains analyzed in sample SC1-1 were larger (mostly 100–200 μm) and had more prismatic grains with aspect ratios as high as 3:1 (Figure 4a). The zircon grains showed poor roundness and more angularity, implying short-distance transport. The CL images revealed (Figure 4a) that most zircon grains showed the fine oscillatory zoning typical of growth in a magmatic environment. On the other hand, some zircons with

inherited cores showed a variable CL response, which is commonly associated with one or more overgrowths. Th/U ratios along with CL images are widely used to determine zircon origin. All zircon grains in this study had a Th/U ratio greater than 0.1 (Figure 4b), which is typical of a magmatic origin.

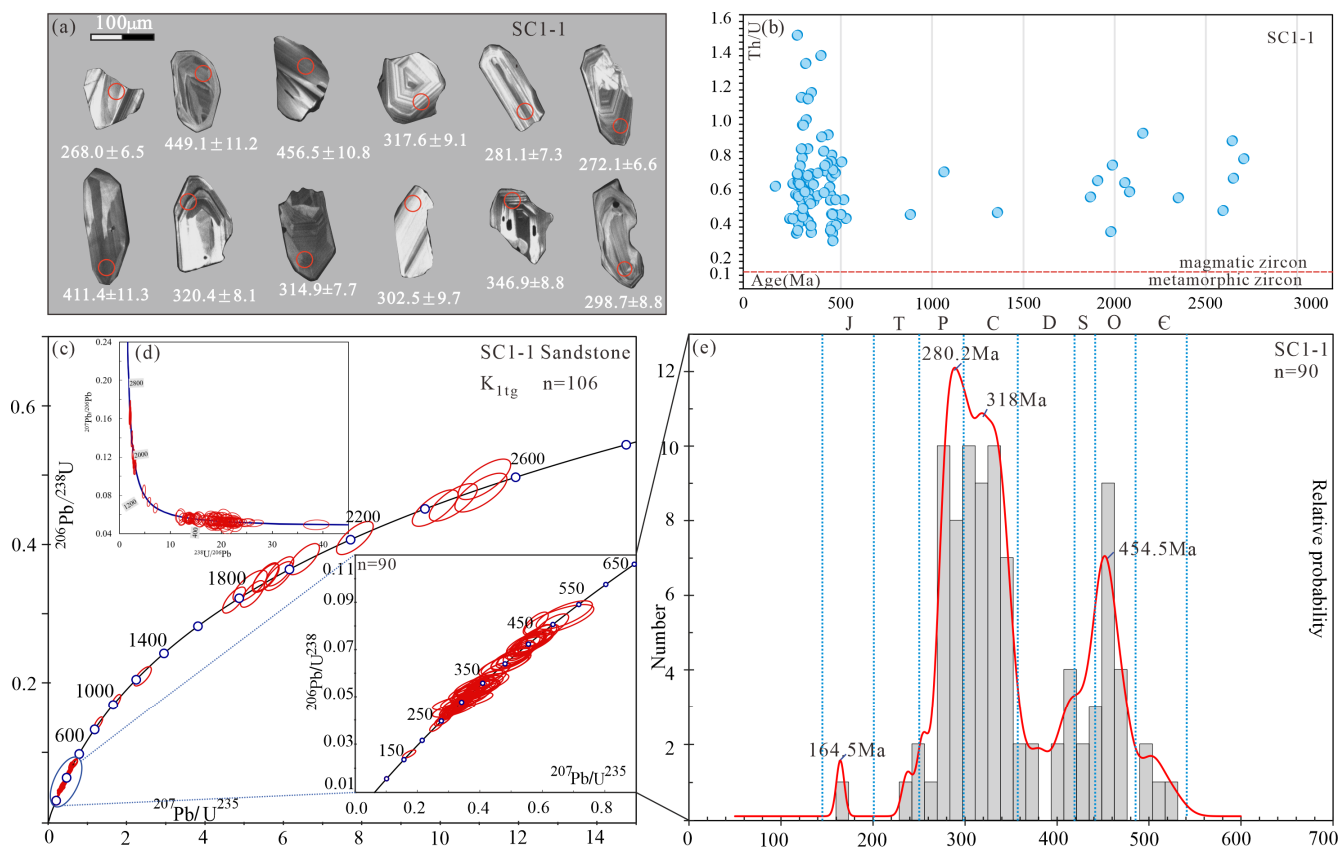


Figure 4. (a) Representative cathodoluminescence images of analyzed grains, (b) plots of Th/U ratios versus U-Pb ages of concordant detrital zircons, (c) zircon U-Pb concordia plots, (d) inverse concordia diagrams (Tera–Wasserburg), and (e) detrital-zircon kernel density estimate (KDE) diagrams.

Sample SC1-1 was obtained from the Tugulu Group. It is evident from the traditional concordance diagram, the Tera–Wasserburg concordance diagram, and Supplementary Table S1 that 107 (99%) of the 108 analyzed grains were concordant, with a high degree of concordance (Figure 4c,d). The U-Pb ages ranged from 164.5 ± 4.3 Ma to 2494.8 ± 35.5 Ma, with ages being primarily concentrated in the Ordovician–Permian. The kernel density estimates of the data exhibited a typical multi-peak age distribution, with three major age peaks at 280.2 Ma and 318 Ma and subordinate peak spectral ages of 454.5 Ma and 164.5 Ma (Figure 4c–e).

4.2. Statistical Comparisons

We could infer the source–sink relationship among the Tupan-Hami and Junggar basins, and the surrounding mountain belts by systematically comparing the detrital-zircon datasets collected from the Late Mesozoic samples in eastern Tien Shan with the reported ages of potential source terranes.

4.2.1. Early Jurassic

Samples JJS-12, JJS-13, and SXG-6 from the Badaowan Formation, along the northern piedmont of the western segment of Bogda, had similar age-distribution patterns and showed Carboniferous, Permian, and pre-Carboniferous peaks, as well as high p -values in the KS tests, 0.950, 1, and 0.957, respectively (Figures 5 and 6), and short distances in

the multidimensional distribution (Figure 7). Therefore, the three samples had similar sources. Sample TS12-86 from the northwest piedmont of Bogda, and Hao-02 and XJ09-097 from the western part of northern Tien Shan had similar age kernel density distributions, with the Carboniferous being the major age peak. In contrast, the Hao-02 sample from the Toutunhe section had a greater proportion of Carboniferous zircon ages than the TS12-86 and XJ09-097 samples (Figure 5). The pre-Carboniferous zircon ages were nearly identical between samples TS12-86 and XJ09-097, and the closer proximity and high p -value (0.606) were evidence of the same source (Figures 6 and 7).

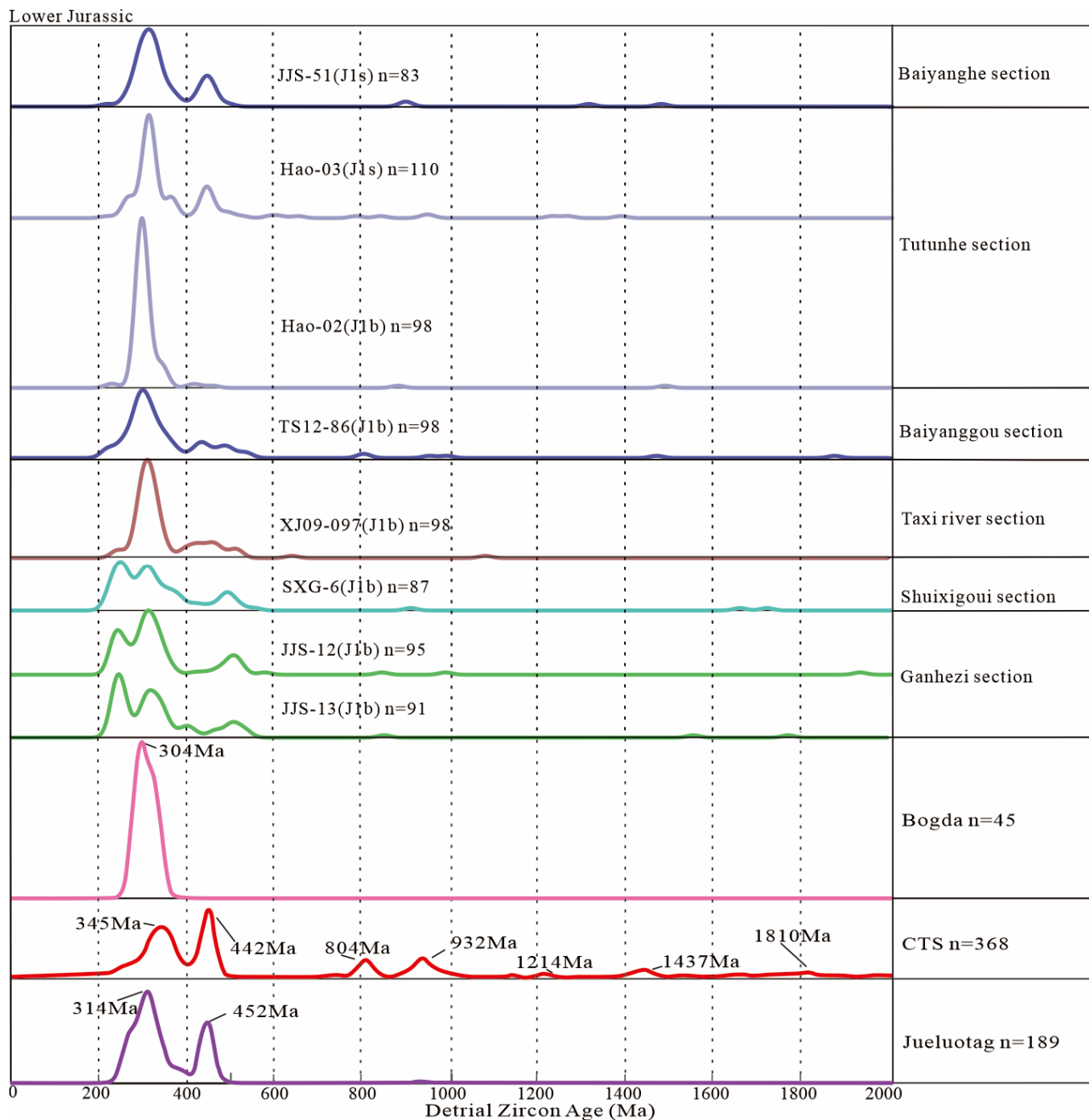


Figure 5. Relative probability map of U-Pb ages of Early Jurassic detrital zircons (data from [23,25,33,35,63]); for map locations, see Figures 1c and 3. Age spectra of potential-source-area features (data from [64,65,68,74] and references therein).

| | JJS-13 | JJS-12 | SXG-6 | Hao-02 | Hao-03 | TS12-86 | JJS-51 | XJ09-097 | Jueluotag | CTS | Bogda |
|-----------|--------|--------|-------|--------|--------|---------|--------|----------|-----------|-------|-------|
| JJS-13 | | 0.950 | 1.000 | 0.000 | 0.001 | 0.039 | 0.001 | 0.000 | 0.003 | 0.000 | 0.002 |
| JJS-12 | 0.950 | | 0.957 | 0.000 | 0.001 | 0.408 | 0.023 | 0.009 | 0.075 | 0.000 | 0.018 |
| SXG-6 | 1.000 | 0.957 | | 0.000 | 0.000 | 0.102 | 0.003 | 0.001 | 0.013 | 0.000 | 0.001 |
| Hao-02 | 0.000 | 0.000 | 0.000 | | 0.000 | 0.000 | 0.000 | 0.000 | 0.000 | 0.000 | 0.205 |
| Hao-03 | 0.001 | 0.001 | 0.000 | 0.000 | | 0.004 | 0.391 | 0.049 | 0.081 | 0.000 | 0.000 |
| TS12-86 | 0.039 | 0.408 | 0.102 | 0.000 | 0.004 | | 0.585 | 0.606 | 0.162 | 0.000 | 0.000 |
| JJS-51 | 0.001 | 0.023 | 0.003 | 0.000 | 0.391 | 0.585 | | 0.856 | 0.932 | 0.000 | 0.001 |
| XJ09-097 | 0.000 | 0.009 | 0.001 | 0.000 | 0.049 | 0.606 | 0.856 | | 0.628 | 0.000 | 0.013 |
| Jueluotag | 0.003 | 0.075 | 0.013 | 0.000 | 0.081 | 0.162 | 0.932 | 0.628 | | 0.000 | 0.000 |
| CTS | 0.000 | 0.000 | 0.000 | 0.000 | 0.000 | 0.000 | 0.000 | 0.000 | 0.000 | | 0.000 |
| Bogda | 0.002 | 0.018 | 0.001 | 0.205 | 0.000 | 0.000 | 0.001 | 0.013 | 0.000 | 0.000 | |

Figure 6. KS P-values tests for Early Jurassic samples (same derived data as those in Figure 5; 95% confidence that the two groups were not statistically different; p -values had to exceed 0.05; comparisons between units with p -values greater than 0.05 are highlighted in yellow).

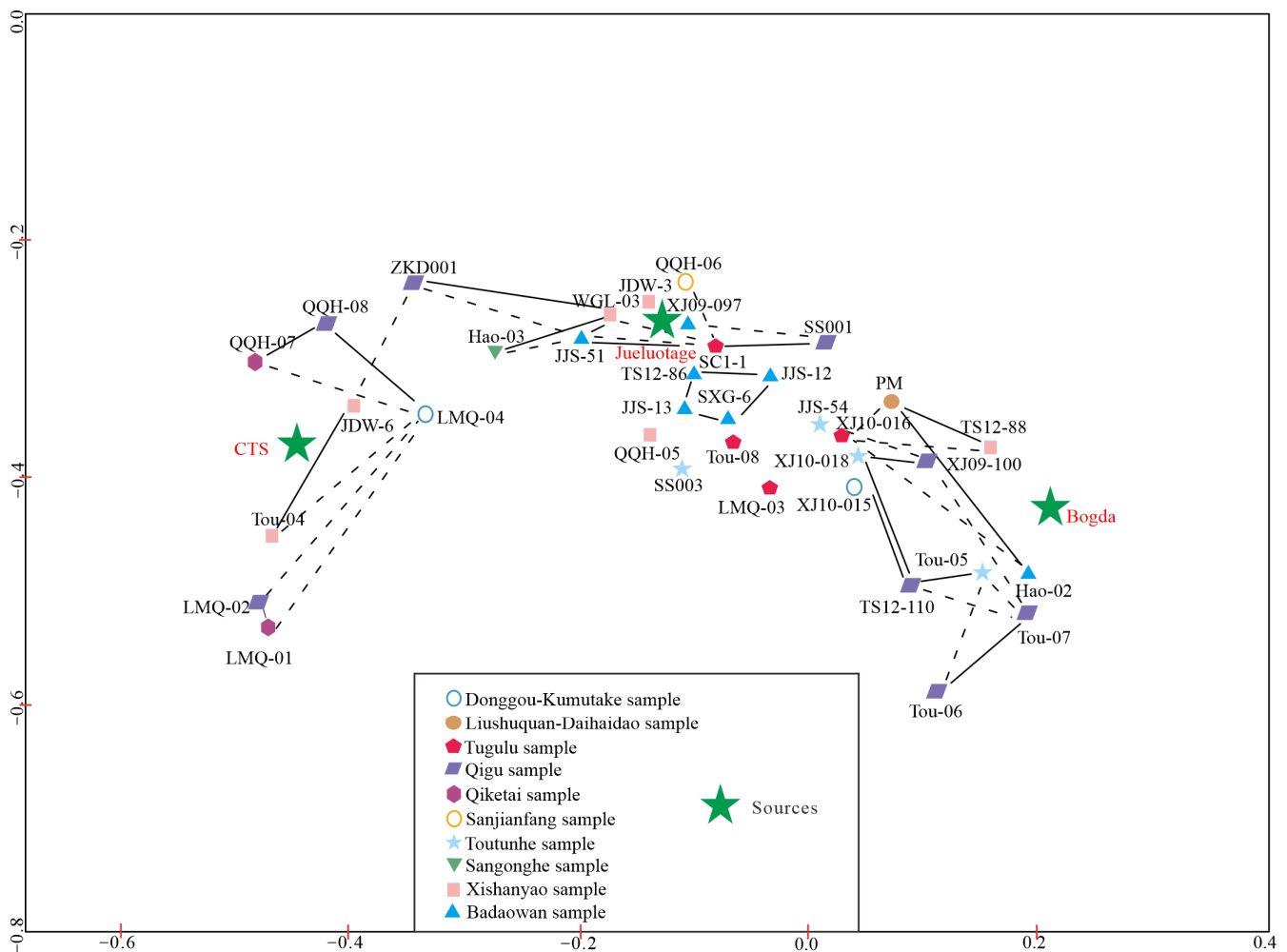


Figure 7. Multidimensional scaling (MDS) diagram of the study samples (data from [23–26,33,35,43,63–65,68,74,103] and this study).

Compared with the samples from the Badaowan Formation in the northern and northwestern piedmont of Bogda and the western section of northern Tien Shan, the Permian-age percentage of the samples collected from the northern piedmont of Bogda accounted for a greater proportion (Figure 5). On the contrary, the Permian ages of the samples from the northwestern piedmont of Bogda and the western section of northern

Tien Shan were significantly less represented, especially for the samples from the western section of northern Tien Shan, which were almost negligible (Figure 5).

In other words, there was a shift in provenance between samples from east to west, as supported by KS tests with high p -values (0.408) for JJS12 and TS12-86 and low p -values (0) for JJS12 and Hao-02, as well as the MDS plots, implying the reactivation of early Mesozoic magmatism in the central Tien Shan region [65] or recycled from Triassic clastic rocks (Figures 6 and 7) [34]. Sample Hao-02 from the Toutunhe section had a high p -value (0.205) in the KS test of the Bogda source region, while the rest of the samples had p -values less than 0.05 in the KS test for the Bogda source (Figure 6). The presence of pre-Carboniferous-age zircons also implied that Bogda did not experience an uplift at this time. The provenance of the samples from the northern piedmont of Bogda probably came from the Qitai paleo uplift or central Tien Shan.

Samples from the Sangonghe and the Badaowan Formations had similar kernel density distributions with Carboniferous-age and Ordovician-age peaks, and the Permian ages almost disappeared (Figure 5). The Ordovician ages increased at this time, with samples JJS-51 and Hao-03 being slightly distant from the others in the multidimensional distribution (Figure 7). High p -values and low p -values were present in the KS tests (0.391, 0.004, etc.; Figure 6), implying a provenance shift or new current provenance incorporation. This feature supports the view that Bogda experienced no uplift during the Early Jurassic.

4.2.2. Middle Jurassic

The kernel density distribution differed between the early and late Xishanyao Formation samples, and sample JDW-3 was dominated by Carboniferous ages, with a sub-peak of pre-Carboniferous ages. Sample JDW-6 was dominated by Ordovician ages and had a sub-peak of Carboniferous ages (Figure 8). The KS tests for samples JDW-3 and JDW-6 showed low p -values (0) (Figure 9) and distances in the multidimensional distribution plot (Figure 7), implying that they had different provenances. Samples JDW-3, WGL-03, and QQH-05 from the northern and southern piedmonts of Bogda had similar multi-peak age spectra. However, QQH-05 was dominated by the Permian, with the Ordovician as the subordinate peak (Figure 8). In the KS tests, WGL-03 and JDW-3 had high p -values (0.1), while QQH-05 had low p -values with respect to JDW-3 and WGL-03, i.e., 0 and 0.026 (Figure 9). Therefore, we argue that QQH-05 had a provenance different from the other two samples, and the multidimensional distribution plot had sub-conclusions (Figure 7).

Visually, sample JDW-6 had a kernel density distribution relatively similar to that of Tou-04; yet, sample Tou-04 also showed a subordinate Permian peak, and JDW-6 had an increased proportion of Carboniferous zircons (Figure 8). The low p -value (0.021) in the KS tests and the distances in the multidimensional distribution plot led us to conclude that the two had different provenances (Figures 7 and 9). Sample TS12-88 from the northwestern piedmont of Bogda had a Carboniferous unimodal distribution pattern (Figure 8), which may be a signal of intense uplift in Bogda. It showed a high p -value (0.607) in the KS tests for Bogda (Figure 9), further confirming that an uplift occurred in the western part of Bogda during this period and that the Tuha and Junggar basins prototypes began to emerge.

Sample QQH-06 from the Sanjianfang Formation had a distribution pattern like that of TS12-88. The difference was that sample QQH-06 had a higher proportion of Ordovician ages (Figure 8). It may have resulted from incorporating a small number of sources from Jueluotag. The high p -value (0.105) in the KS tests (Figure 9) confirmed that the Jueluotag source area was ascribable for the provenance of the northern part of the basin. Sample LMQ-01 from the Qiketai Formation in the Lianmuqin section had dominant and subdominant peaks opposite to those of its contemporaries in the Qiquanhu section, with a dominant Ordovician peak and a subdominant Permian peak accompanied by a small number of Precambrian ages (Figure 8), which was mainly attributed to its close position to the Jueluotag and central Tien Shan source areas, implying a slight uplift in the central segment of Bogda.

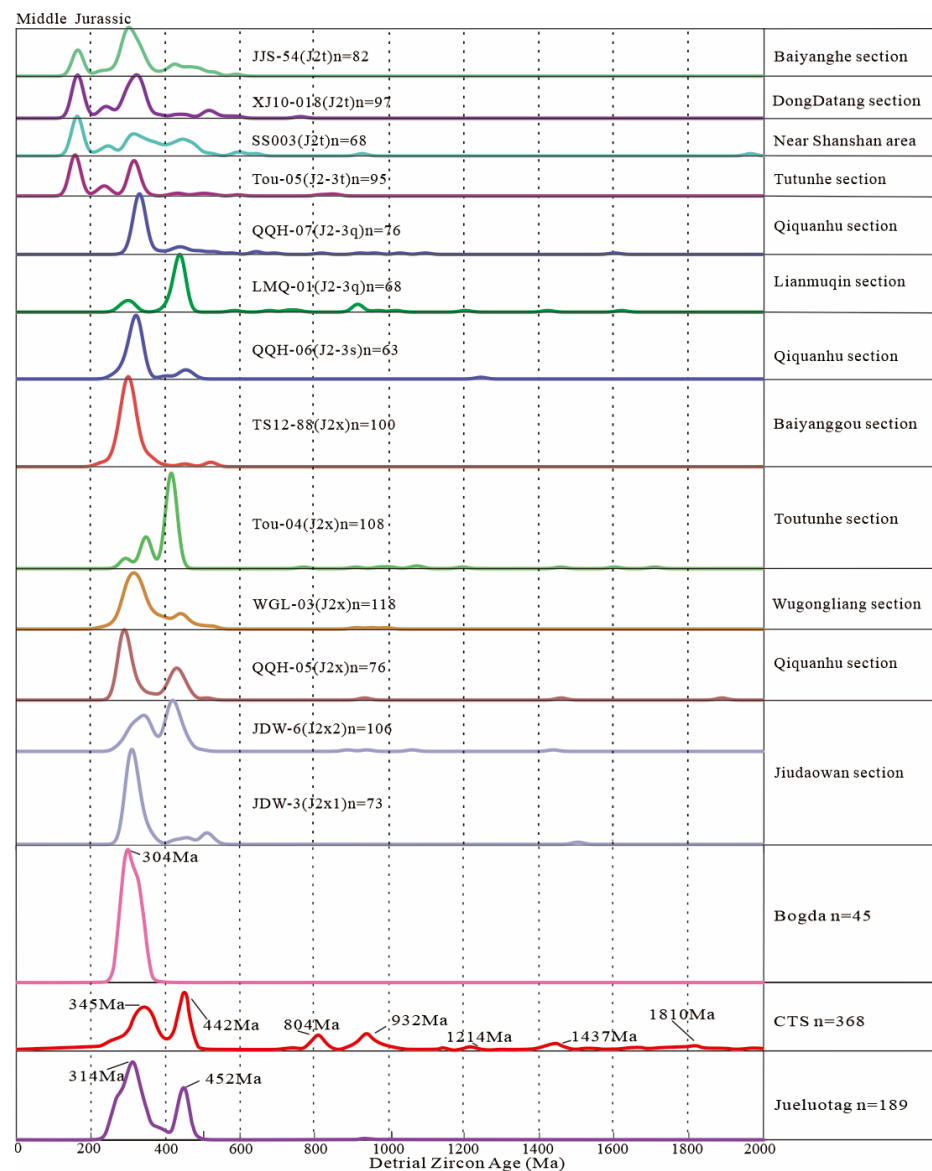


Figure 8. Relative probability map of U-Pb ages of Middle Jurassic detrital zircons (data from [23,24,26,33,35,43,63]); for map locations, see Figures 1c and 3. Age spectra of potential-source-area features (data from [64,65,68,74] and references therein).

| | OOH-05 | WGL-03 | JDW-3 | JDW-6 | Tou-04 | TS12-88 | SS003 | XJ10-018 | JJS-54 | Jueluotag | CTS | Bogda |
|-----------|--------|--------|-------|-------|--------|---------|-------|----------|--------|-----------|-------|-------|
| OOH-05 | | 0.026 | 0.000 | 0.000 | 0.000 | 0.001 | 0.000 | 0.000 | 0.045 | 0.054 | 0.000 | 0.000 |
| WGL-03 | 0.026 | | 0.100 | 0.000 | 0.000 | 0.000 | 0.000 | 0.000 | 0.015 | 0.500 | 0.000 | 0.000 |
| JDW-3 | 0.000 | 0.100 | | 0.000 | 0.000 | 0.000 | 0.000 | 0.000 | 0.000 | 0.063 | 0.000 | 0.014 |
| JDW-6 | 0.000 | 0.000 | 0.000 | | 0.021 | 0.000 | 0.000 | 0.000 | 0.000 | 0.000 | 0.000 | 0.000 |
| Tou-04 | 0.000 | 0.000 | 0.000 | 0.021 | | 0.000 | 0.000 | 0.000 | 0.000 | 0.000 | 0.000 | 0.000 |
| TS12-88 | 0.001 | 0.000 | 0.000 | 0.000 | 0.000 | | 0.001 | 0.000 | 0.116 | 0.000 | 0.000 | 0.607 |
| SS003 | 0.000 | 0.000 | 0.000 | 0.000 | 0.000 | 0.001 | | 0.016 | 0.214 | 0.000 | 0.000 | 0.000 |
| XJ10-018 | 0.000 | 0.000 | 0.000 | 0.000 | 0.000 | 0.000 | 0.016 | | 0.266 | 0.000 | 0.000 | 0.000 |
| JJS-54 | 0.045 | 0.015 | 0.000 | 0.000 | 0.000 | 0.116 | 0.214 | 0.266 | | 0.013 | 0.000 | 0.034 |
| Jueluotag | 0.054 | 0.500 | 0.063 | 0.000 | 0.000 | 0.000 | 0.000 | 0.000 | 0.013 | | 0.000 | 0.000 |
| CTS | 0.000 | 0.000 | 0.000 | 0.000 | 0.000 | 0.000 | 0.000 | 0.000 | 0.000 | 0.000 | | 0.000 |
| Bogda | 0.000 | 0.000 | 0.014 | 0.000 | 0.000 | 0.607 | 0.000 | 0.000 | 0.034 | 0.000 | 0.000 | |

Figure 9. KS p -value tests for Middle Jurassic samples (same derived data as those in Figure 8; 95% confidence that the two groups were not statistically different; p -values had to exceed 0.05; comparisons between units with p -values greater than 0.05 are highlighted in yellow).

The kernel-density-distribution patterns differed between the samples from the Toutunhe and Xishanyao Formations, with samples from the Toutunhe Formation displaying a similar multimodal distribution pattern, with significant partitioning in the multidimensional distribution plot (Figures 7 and 8). In addition, Jurassic detrital zircons were present, implying contemporaneous volcanism at the southern margin of the Junggar basin. Sample SS003 was less Carboniferous in age than other samples from the western part of northern Tien Shan, primarily due to the onset of an uplift in northern Tien Shan, which prevented the input of sources from the western part of central Tien Shan.

In contrast, no uplift occurred in the central segment of Bogda, and a weak uplift possibly occurred in the eastern segment. The appearance of Jurassic ages in the age spectra of samples from the interior of the basin may have been the result of earlier stratigraphic recycling (Figure 8) or the possibility that volcanic materials from the southern margin of the Junggar basin could still be transported into the interior of the Tuha basin, implying that the uplift of the western segment of Bogda was not active. However, there was a hindering factor for source transport. The high proportion of pre-Carboniferous ages inside the basin implied that the uplift was more intense in central Tien Shan and Jueluotag.

4.2.3. Late Jurassic

Samples from the Qigu and Toutunhe Formations, derived from the northwestern piedmont of Bogda and the western part of northern Tien Shan, had a similar kernel-density-distribution pattern, featuring Jurassic, Triassic, and pre-Carboniferous peaks (Figure 10). It can be noticed that the proportion of Jurassic zircons decreased in samples away from the southern margin of the Junggar basin (XJ09-100). That means that volcanic activity was still ongoing at the southern margin of the Junggar basin and getting farther away, with less availability of volcanic materials. In the Qiquanhu section, the age spectrum of sample QQH-08 was more like those of samples collected from the Qiketai Formation in this section (Figures 10 and 11). However, there was a slight increase in the proportion of pre-Carboniferous ages. It may be attributed to more abundant sources in Jueluotag and in the central segment of Bogda, which was supported by the distance between the two samples, and Jueluotag and Bogda in the multidimensional distribution plot (Figure 7). Samples LMQ-02 and LMQ-01 from the Lianmuqin section had almost identical age spectra and high KS-test values (0.954) (Figure 11). They were closer to the central Tien Shan source in the multidimensional distribution (Figure 7), implying that the source area was almost identical for them. The origin may have been central Tien Shan or Bogda.

Samples SS001 and ZKD001, from the eastern and western basin sides, had bimodal age spectra (Figure 10). However, the eastern side of the basin had a greater proportion of pre-Carboniferous ages for sample ZKD001, suggesting a decreasing quantity of Jueluotag sources towards the basin's western side. The samples collected from the Toutunhe section showed an increased proportion of Carboniferous ages and a lower proportion of pre-Carboniferous ages during the development of the Kalaza Formation (Figure 10), confirming that the eastern and western segments of Bogda experienced an uplift in this period. Sample LMQ-02 showed a lesser Carboniferous age, suggesting that the eastern section of central Tien Shan could still cross Jueluotag to feed the basin. The lower proportion of zircons of pre-Carboniferous ages in the western part of the northern Tien Shan samples implied that the northern Tien Shan uplift was intense later, preventing sources from the western part of central Tien Shan. The KS tests also showed a high *p*-value (0.229) for Bogda with respect to SS001, implying that a larger-scale uplift occurred in the central segment of Bogda.

To summarize, a large-scale uplift occurred in Bogda, with numerous sources being transported into the basin (Figures 10 and 11). It should not be overlooked that the sample age spectrum of the basin alone did not show Jurassic ages (Figure 10); this also shows that Bogda separated the Tuha and Junggar basins.

Upper Jurassic

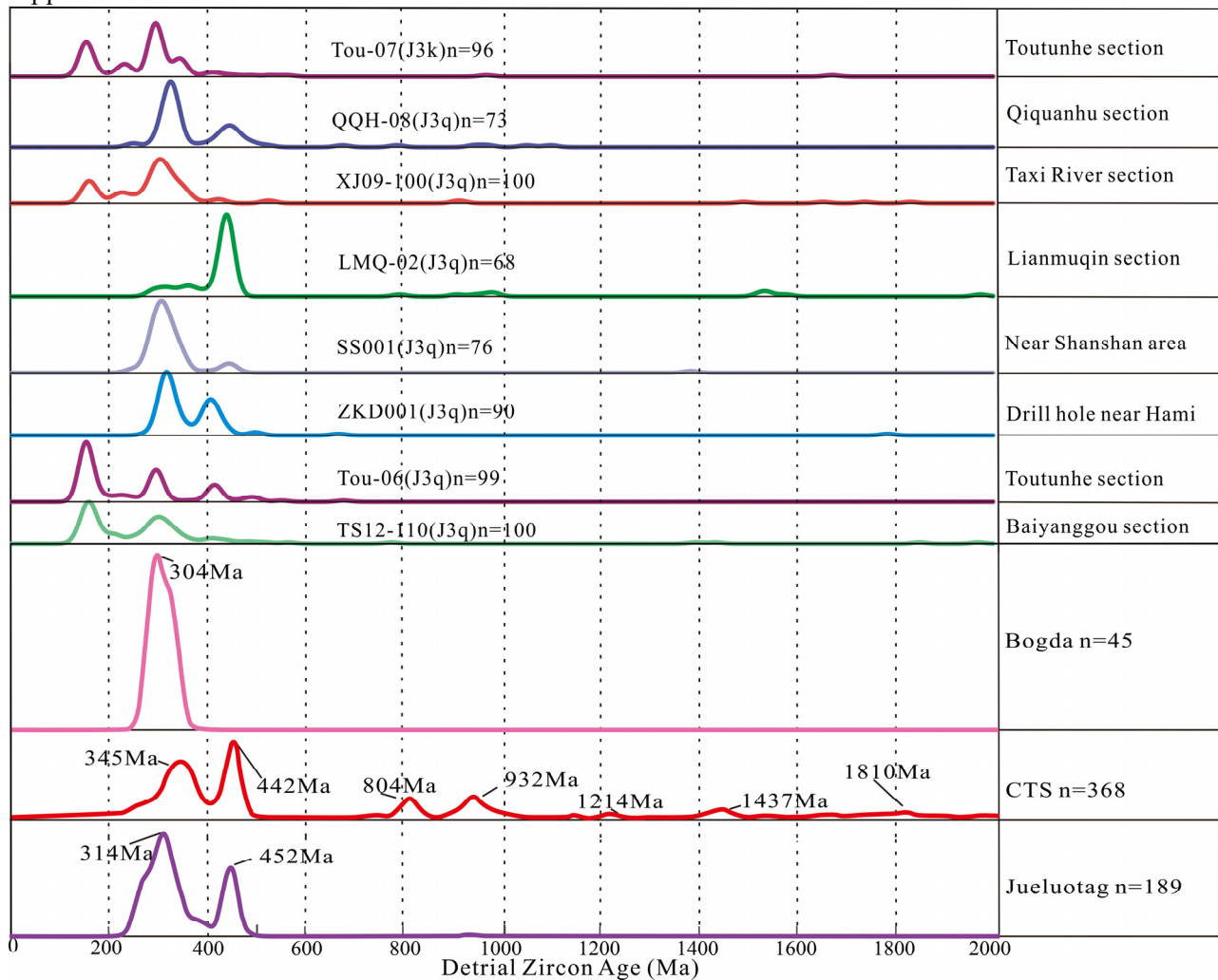


Figure 10. Relative probability map of U-Pb ages of detrital zircons from Late-Middle-Jurassic to Late Jurassic (data from [23,24,35,43,63]); for map locations, see Figures 1c and 3. Age spectra of potential-source area features (the data from [64,65,68,74] and references therein).

| | QQH-06 | Tou-05 | LMQ-01 | QQH-07 | TS12-110 | Tou-06 | ZKD001 | SS001 | LMQ-02 | XJ09-100 | QQH-08 | Tou-07 | Jueluotag | CTS | Bogda |
|-----------|--------------|--------------|--------------|--------------|--------------|--------------|--------------|--------------|--------------|----------|--------------|--------------|--------------|-------|--------------|
| QQH-06 | | 0.000 | 0.000 | 0.002 | 0.000 | 0.000 | 0.015 | 0.138 | 0.000 | 0.001 | 0.012 | 0.000 | 0.105 | 0.000 | 0.013 |
| Tou-05 | 0.000 | | 0.000 | 0.000 | 0.555 | 0.025 | 0.000 | 0.000 | 0.000 | 0.007 | 0.000 | 0.143 | 0.000 | 0.000 | 0.000 |
| LMQ-01 | 0.000 | 0.000 | | 0.000 | 0.000 | 0.000 | 0.000 | 0.000 | 0.954 | 0.000 | 0.000 | 0.000 | 0.000 | 0.004 | 0.000 |
| QQH-07 | 0.002 | 0.000 | 0.000 | | 0.000 | 0.000 | 0.130 | 0.000 | 0.000 | 0.000 | 0.950 | 0.000 | 0.000 | 0.000 | 0.000 |
| TS12-110 | 0.000 | 0.555 | 0.000 | 0.000 | | 0.122 | 0.000 | 0.000 | 0.000 | 0.030 | 0.000 | 0.200 | 0.000 | 0.000 | 0.000 |
| Tou-06 | 0.000 | 0.025 | 0.000 | 0.000 | 0.122 | | 0.000 | 0.000 | 0.000 | 0.000 | 0.000 | 0.012 | 0.000 | 0.000 | 0.000 |
| ZKD001 | 0.015 | 0.000 | 0.000 | 0.130 | 0.000 | 0.000 | | 0.000 | 0.000 | 0.000 | 0.023 | 0.000 | 0.006 | 0.000 | 0.000 |
| SS001 | 0.138 | 0.000 | 0.000 | 0.000 | 0.000 | 0.000 | 0.000 | | 0.000 | 0.002 | 0.000 | 0.000 | 0.013 | 0.000 | 0.229 |
| LMQ-02 | 0.000 | 0.000 | 0.954 | 0.000 | 0.000 | 0.000 | 0.000 | 0.000 | | 0.000 | 0.000 | 0.000 | 0.000 | 0.000 | 0.000 |
| XJ09-100 | 0.001 | 0.007 | 0.000 | 0.000 | 0.030 | 0.000 | 0.000 | 0.002 | 0.000 | | 0.000 | 0.038 | 0.000 | 0.000 | 0.007 |
| QQH-08 | 0.012 | 0.000 | 0.000 | 0.950 | 0.000 | 0.000 | 0.023 | 0.000 | 0.000 | 0.000 | | 0.000 | 0.002 | 0.000 | 0.000 |
| Tou-07 | 0.000 | 0.143 | 0.000 | 0.200 | 0.012 | 0.000 | 0.000 | 0.000 | 0.000 | 0.038 | 0.000 | | 0.000 | 0.000 | 0.000 |
| Jueluotag | 0.105 | 0.000 | 0.000 | 0.000 | 0.000 | 0.000 | 0.006 | 0.013 | 0.000 | 0.000 | 0.002 | 0.000 | | 0.000 | 0.000 |
| CTS | 0.000 | 0.000 | 0.004 | 0.000 | 0.000 | 0.000 | 0.000 | 0.000 | 0.000 | 0.000 | 0.000 | 0.000 | 0.000 | | 0.000 |
| Bogda | 0.013 | 0.000 | 0.000 | 0.000 | 0.000 | 0.000 | 0.000 | 0.229 | 0.000 | 0.007 | 0.000 | 0.000 | 0.000 | 0.000 | |

Figure 11. KS P-value tests for late Middle Jurassic–Late Jurassic samples (same derived data as those in Figures 8 and 10; 95% confidence that the two groups were not statistically different; *p*-values had to exceed 0.05; comparisons between units with *p*-values greater than 0.05 are highlighted in yellow).

4.2.4. Cretaceous

The PM series of the Early Cretaceous samples collected at the basin had similar age-distribution patterns (Figure 12), implying a similar provenance. The KS tests also displayed that they had high p -values with respect to each other (0.198, 0.825, 0.982, 0.961, etc.) (Figure 13). The near disappearance of the Precambrian ages (Figure 11) indicated that central Tien Shan was no longer feeding the basin across Jueluotag, and the KS tests yielded low quality (0) (Figure 13), further confirming that central Tien Shan was no longer feeding the basin. In comparison to sample ZKD001, the decrease in pre-Carboniferous ages (Figure 12) suggests that the provenance of Jueluotag also decreased. The PM series of samples had the most significant proportion of Carboniferous ages, with proportions upwards of 80%.

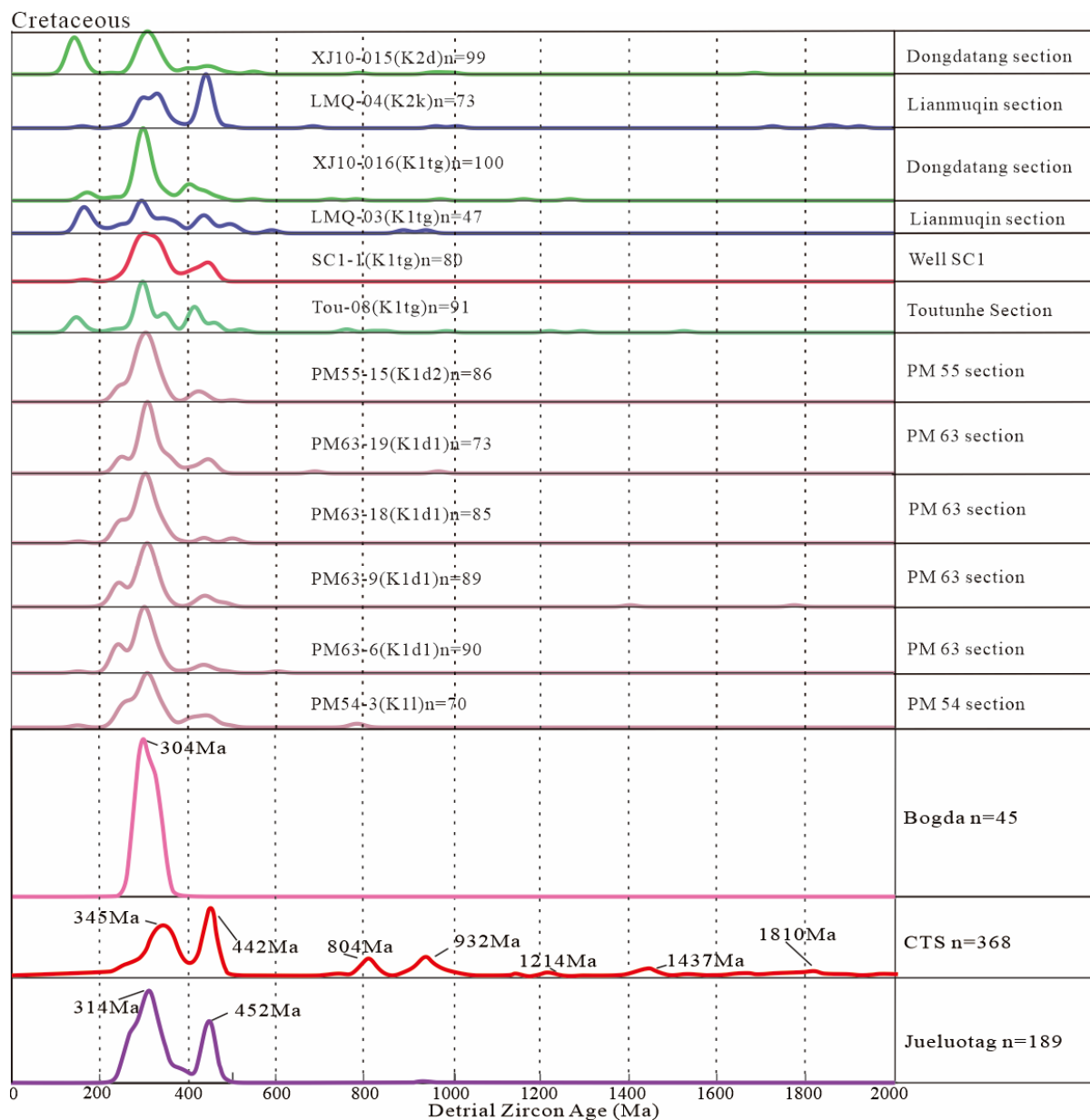


Figure 12. Relative probability map of U-Pb ages of Cretaceous detrital zircons (data from [24,43,63] and this study); for map locations, see Figures 1c and 3. Age spectra of potential-source-area features (data from [64,65,68,74] and references therein).

| | PM54-3 | PM63-6 | PM63-9 | PM63-18 | PM63-19 | PM55-15 | Tou-08 | SC1-1 | LMQ-03 | XJ10-016 | LMQ-04 | XJ10-015 | Jueluotag | CTS | Bogda |
|-----------|--------|--------|--------|---------|---------|---------|--------|-------|--------|----------|--------|----------|-----------|-------|-------|
| PM54-3 | | 0.198 | 0.825 | 0.411 | 0.715 | 0.563 | 0.221 | 0.693 | 0.132 | 0.678 | 0.000 | 0.002 | 0.149 | 0.000 | 0.054 |
| PM63-6 | 0.198 | | 0.284 | 0.982 | 0.004 | 0.317 | 0.000 | 0.006 | 0.015 | 0.164 | 0.000 | 0.001 | 0.000 | 0.000 | 0.058 |
| PM63-9 | 0.825 | 0.284 | | 0.846 | 0.455 | 0.961 | 0.003 | 0.077 | 0.078 | 0.527 | 0.000 | 0.000 | 0.006 | 0.000 | 0.236 |
| PM63-18 | 0.411 | 0.982 | 0.846 | | 0.037 | 0.880 | 0.001 | 0.014 | 0.020 | 0.094 | 0.000 | 0.001 | 0.000 | 0.000 | 0.218 |
| PM63-19 | 0.715 | 0.004 | 0.455 | 0.037 | | 0.160 | 0.191 | 0.539 | 0.074 | 0.057 | 0.000 | 0.001 | 0.110 | 0.000 | 0.029 |
| PM55-15 | 0.563 | 0.317 | 0.961 | 0.880 | 0.160 | | 0.001 | 0.030 | 0.031 | 0.160 | 0.000 | 0.000 | 0.002 | 0.000 | 0.541 |
| Tou-08 | 0.221 | 0.000 | 0.003 | 0.001 | 0.191 | 0.001 | | 0.348 | 0.484 | 0.199 | 0.004 | 0.032 | 0.010 | 0.000 | 0.000 |
| SC1-1 | 0.693 | 0.006 | 0.077 | 0.014 | 0.539 | 0.030 | 0.348 | | 0.064 | 0.142 | 0.000 | 0.001 | 0.309 | 0.000 | 0.004 |
| LMQ-03 | 0.132 | 0.015 | 0.078 | 0.020 | 0.074 | 0.031 | 0.484 | 0.064 | | 0.147 | 0.014 | 0.090 | 0.009 | 0.000 | 0.002 |
| XJ10-016 | 0.678 | 0.164 | 0.527 | 0.094 | 0.057 | 0.160 | 0.199 | 0.142 | 0.147 | | 0.000 | 0.002 | 0.000 | 0.000 | 0.013 |
| LMQ-04 | 0.000 | 0.000 | 0.000 | 0.000 | 0.000 | 0.000 | 0.004 | 0.000 | 0.014 | 0.000 | | 0.000 | 0.001 | 0.000 | 0.000 |
| XJ10-015 | 0.002 | 0.001 | 0.000 | 0.001 | 0.001 | 0.000 | 0.032 | 0.001 | 0.090 | 0.002 | 0.000 | | 0.000 | 0.000 | 0.004 |
| Jueluotag | 0.149 | 0.000 | 0.006 | 0.000 | 0.110 | 0.002 | 0.010 | 0.309 | 0.009 | 0.000 | 0.001 | 0.000 | | 0.000 | 0.000 |
| CTS | 0.000 | 0.000 | 0.000 | 0.000 | 0.000 | 0.000 | 0.000 | 0.000 | 0.000 | 0.000 | 0.000 | 0.000 | 0.000 | | 0.000 |
| Bogda | 0.054 | 0.058 | 0.236 | 0.218 | 0.029 | 0.541 | 0.000 | 0.004 | 0.002 | 0.013 | 0.000 | 0.004 | 0.000 | 0.000 | |

Figure 13. KS P-value tests for Cretaceous samples (same derived data as those in Figure 12; 95% confidence that the two groups were not statistically different; *p*-values had to exceed 0.05; comparisons between units with *p*-values greater than 0.05 are highlighted in yellow).

From the analyses with the KS tests, almost all samples inside the basin had high *p*-values with respect to Bogda, i.e., 0.054, 0.058, 0.236, 0.218 and 0.541 (Figure 13). Following a visual comparison, the age spectra of the PM series samples were roughly morphologically like those of sample SC1-1. However, SC1-1 showed a more broadly bimodal age spectrum (Figure 12). Although they had similar sources, this explained the differences between the SC1-1 and PM series samples, and the multidimensional distribution plots confirmed the differences (Figure 12). Each PM series subsample and sample SC1-1 had different *p*-values according to the KS tests.

Compared with the PM series of samples from the basin, the samples from the Tugulu Group in the western part of northern Tien Shan had similar distributions of Paleozoic ages. However, the western part of the northern Tien Shan samples also had a Jurassic-age peak (Figure 12). It was mainly the result of the relatively intense and long-active volcanism at the southern margin of the Junggar basin during the Jurassic; subsequently, massive tuffs deposited. From the Early Jurassic to the Cretaceous, the proportion of pre-Carboniferous ages gradually decreased, and the proportion of Carboniferous and Permian ages grew (Figure 12), indicating the declining feeding capabilities of central Tien Shan and Jueluotag. Sample LMQ-03 from the Lianmuqin section was more obvious than LMQ-01 and LMQ-02. It was also evident that samples LMQ-01 and LMQ-02 were closer to the central Tien Shan source than sample LMQ-03 in the multidimensional distribution plot (Figure 12). All the above evidence indicates that the central Tien Shan source decreased in availability.

The significant difference in the age spectra of samples LMQ-04 and LMQ-03 implied that the two had different provenances (Figure 12). The low *p*-value (0.014) in the KS tests for both supported this conclusion (Figure 13). From the development of the Kalaza Formation to that of the Tugulu Group, there was a significant reduction in source feed from the western part of central Tien Shan. Sample LMQ-04 had more pre-Carboniferous and Carboniferous ages and lacked Mesozoic ages (Figure 12), which was mainly caused by the re-activation of the eastern section of the central Tien Shan during the development of the Kumutake Formation. The Jurassic stratigraphic recycling was in the western part of the basin during the development of the Tugulu Group and declined with the development of the Kumutake Formation. The absence of Mesozoic ages in the PM series suggested that no Jurassic stratigraphic recycling occurred in the eastern part of the basin.

Samples XJ10-015 and XJ10-016 both had Jurassic ages, meaning the renewed erosion of the southern margin of the Junggar basin and the shrinking of the lake pool [40]. However, sample XJ10-015 had a greater proportion of Jurassic ages, suggesting that the Junggar basin was constantly shrinking. The KS tests of all the Cretaceous samples yielded

overwhelmingly high p -values (0.054, 0.058, 0.236, etc.; Figure 13), indicating the affinity of the samples to Bogda and that large-scale uplift of Bogda occurred during this time. The KS tests yielded higher p -values (0.309, 0.110, 0.149; Figure 13) for samples from the eastern part of the basin with respect to Jueluotag, implying that Jueluotag only provided sources for the eastern part of the basin.

5. Discussions

5.1. Quantitatively Determined Source Mixing Proportions: Implication for Multi-Stage Evolution of the Eastern Tien Shan Region

In Central Asia, the Jurassic–Early Cretaceous period corresponded to a transition between two major orogenic belts: the Early Mesozoic–Cimmerian orogeny and the Late Cretaceous–Cenozoic orogeny [55,100]. After the Cimmerian orogeny, the topography of Central Asia was gradually planated [104]. However, studies of the detrital zircons from the eastern Tien Shan region revealed that successive multi-phase tectonic events occurred, such as the segmental differential uplift of Bogda and the turbulent uplift–denudation of central Tien Shan and Jueluotag.

While a simple statistical correlation analysis of detrital zircons and a comparison of the detrital-zircon age spectra of each sample can reveal general source variations, a quantitative study helps to elucidate the exact contribution of eastern Tien Shan region sources through time. We combined available sedimentological and U–Pb thermal chronology datasets, and this information can effectively reveal and help us to understand the Late Mesozoic tectonic evolution of the eastern Tien Shan region. The inverse Monte Carlo model results for each test sample are shown in Figures 14–17, and the relevant remaining data information is listed in Table S3. The results suggested that during the Early Jurassic, Jueluotag and central Tien Shan were the main source regions with 86–100% of the eastern Tien Shan region (Figure 14).

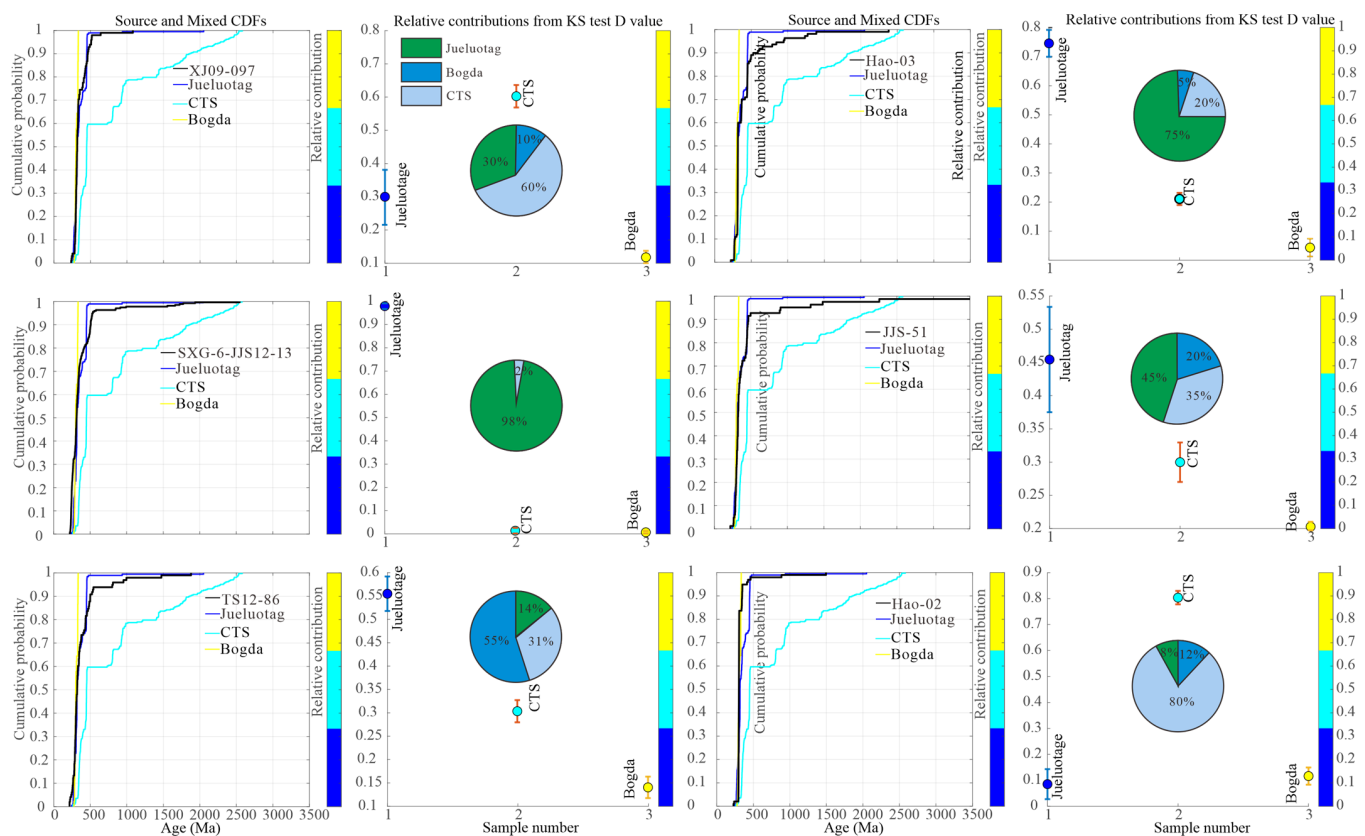


Figure 14. Decomposition model quantifying the U–Pb age distribution of detrital zircons from different source areas using DZ mixed modeling [8]; J1-Dzmix.

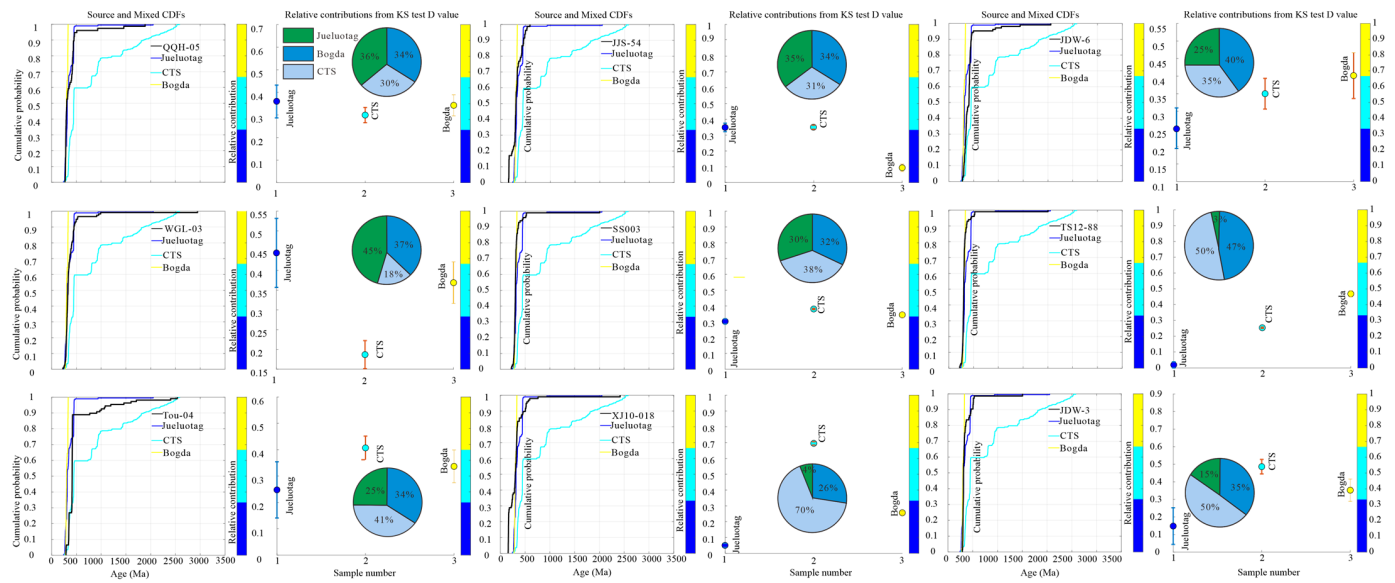


Figure 15. Decomposition model quantifying the U-Pb age distribution of detrital zircons from different source areas using DZ mixed modeling [8]; J2-Dzmix.

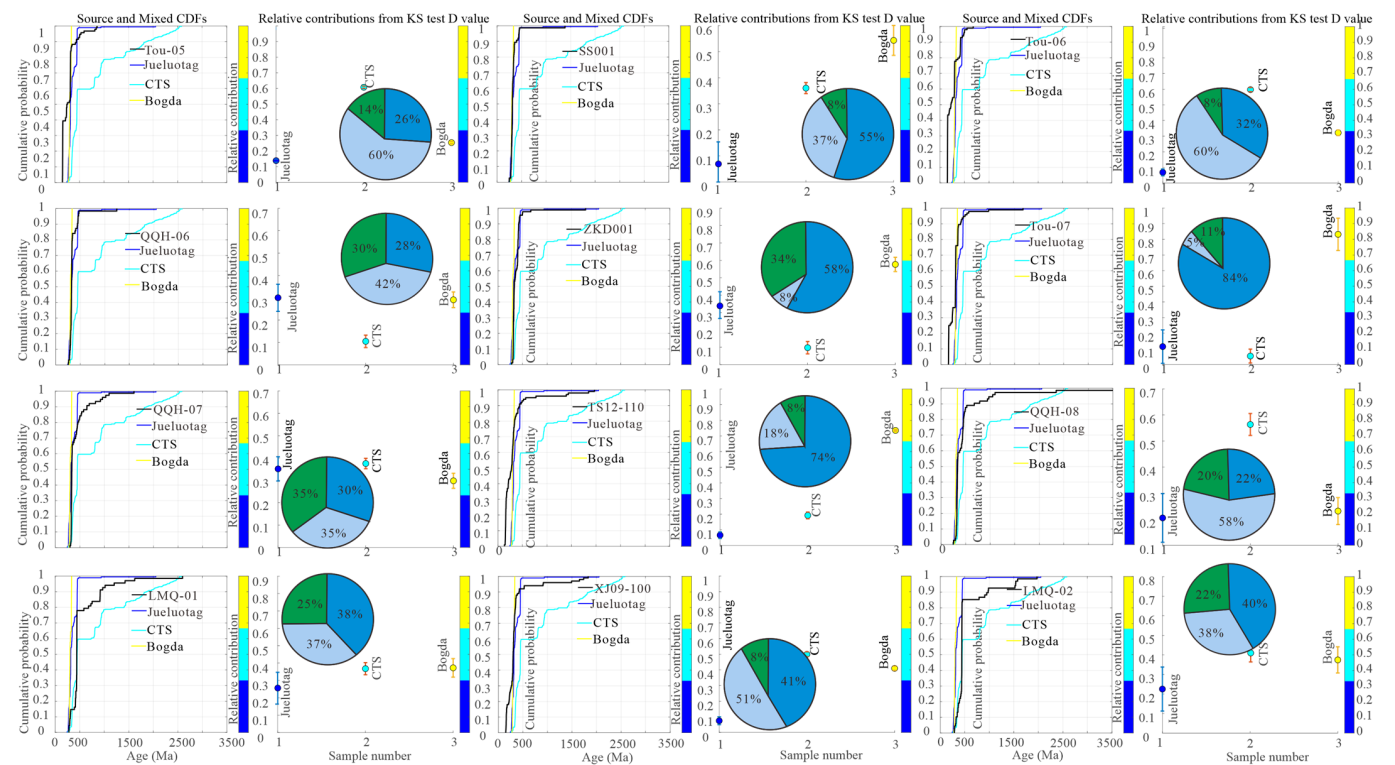


Figure 16. Decomposition model quantifying the U-Pb age distribution of detrital zircons from different source areas using DZ mixed modeling [8]; J2-3-3-Dzmix.

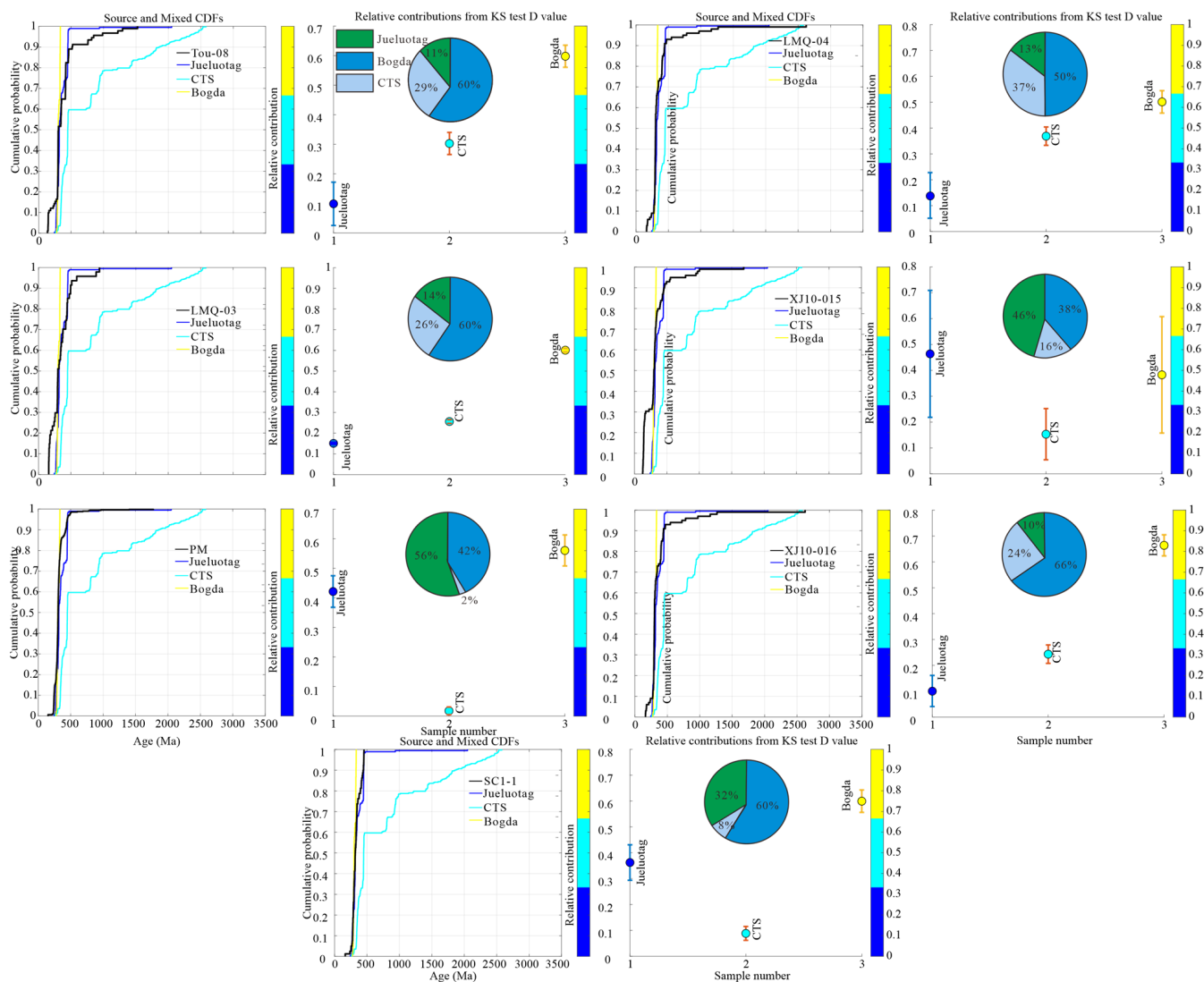


Figure 17. Decomposition model quantifying the U-Pb age distribution of detrital zircons from different source areas using DZ mixed modeling [8]; K-DZmix.

The Early and Middle Jurassic periods were characterized by the development of extensive alluvial-plain-lake environments [32]; the formation of large amounts of coal during these periods indicates a relatively wet climate [32,34,42]. At the southern margin of the Junggar basin, Jurassic strata thicken towards Bogda, and the Jurassic strata, at the northern piedmont of Bogda, mainly consist of alluvial sandstones and alluvial mudstones [28], which is consistent with previous views that Bogda was geographically gentle during the Early Jurassic [25,33,35]. Li et al. [92,105] and Hendrix et al. [32] concluded that Tien Shan was a positive relief from the Early to the Middle Jurassic periods based on the remaining Jurassic strata of central and northern Tien Shan. Therefore, Bogda did not experience an uplift, only as positive topography, the provenance of its adjacent areas being ascribable to it (Figure 18a) [100]. The northern-central parts of the Turpan-Hami basin may have derived from the Qitai paleo-uplift region [42]. Chen et al. [101] found that rapid-cooling events were widespread in eastern and western Tien Shan and in Beishan using low-temperature thermochronology (Figure 3). However, there are no records of Late Triassic exhumation events in the northern Altai region [106], which shows that the Late Triassic–Early Jurassic uplift–denudation of the eastern Tien Shan region was associated with a geodynamic event in the south.

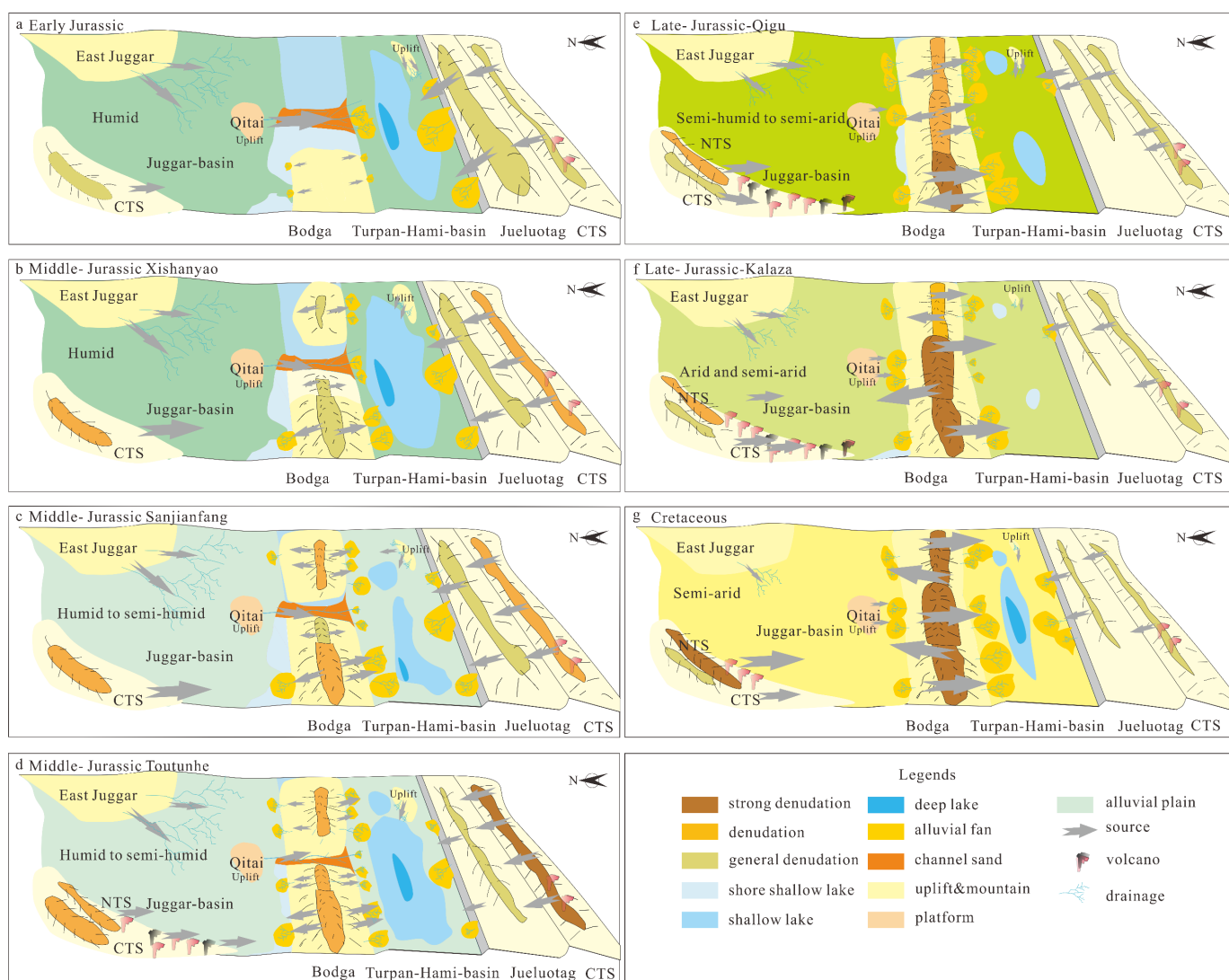


Figure 18. Schematic diagrams (not to scale) illustrating the tectonic evolution of the Turpan-Hami basin and its adjacent regions during the Jurassic–Cretaceous; (a) Early Jurassic; (b) Middle Jurassic-Xishanyao; (c) Middle Jurassic Sanjianfang; (d) Middle Jurassic Toutunhe; (e) Late Jurassic Qigu; (f) Late Jurassic Kalazha; (g) Cretaceous.

During the Middle Jurassic, the primary sources were still Jueluotag and central Tien Shan, with an average proportion of 66.1%. However, the source proportion of Bogda increased to 33.9% compared with the Early Jurassic, from a previous 10.2% (Figure 15). Apatite- and zircon-fission-track ages of 187–171 Ma in adjacent areas [92,97–99] further confirmed the conclusion (Figure 3). By the Late Jurassic, the total proportion of central Tien Shan and Jueluotag was only 49.5%, while for Bogda, the proportion increased to 50.5% (Figure 16). Many studies that analyzed the fission-track dating of Bogda yielded Late Cretaceous and Cenozoic dates [93–95,100], and one study presented a sample from the southwestern margin of Bogda with an age of 152 ± 15 Ma (Figure 3) [96], which also confirms our results. During the Cretaceous, the source proportion of Bogda amounted to 53.7%, which is over half, while the proportion of central Tien Shan and Jueluotag decreased to 46.3% (Figure 17).

In general, during the Early Jurassic, Bogda provided few sources and merely as positive topography. From the Early Jurassic to the Cretaceous, the source proportion of Bogda gradually increased over time, especially with the large-scale uplift and denudation that occurred after the development of the Qigu Formation. Previous studies found that

apatite fission tracks in southwestern Bogda were older, most of them over 100 Ma [100] (Figure 3), and the extensive 187–171 Ma and 150–100 Ma as well as an age of 152 ± 15 Ma cooling recorded in apatite-fission-track data support this uplift background [37,95,97,100] (Figure 3). On the other hand, the Jueluotag and central Tien Shan proportions gradually declined before the Cretaceous. From the Late Jurassic to the Cretaceous, the decreasing tendency of the Jueluotag and central Tien Shan source percentages slowed down, with an increasing trend for Jueluotag. In further analyses, central Tien Shan had a slightly growing trend (41.3%; Figures 14 and 15) from the Early Jurassic to the Middle Jurassic, gradually decreasing to 20.3% (Figures 17 and 18). It still accounted for a sizeable proportion of sources. It is possible that provenance ascribable to the central Tien Shan still crossed the poorly uplifted Jueluotag to the Turpan-Hami basin [96]. Like central Tien Shan, Jueluotag gradually decreased from an initial 51.8% to 14.9% in the Late Jurassic, but the proportion increased again to 26% in the Cretaceous (Figures 14–18).

It is worth noting that Bogda accounted for a higher percentage of western and eastern segments samples (40%, 47%, 37%, 34%) than central segment samples (32%, 28%, etc.), generally during the Middle and Late Jurassic periods (Figures 15, 16 and 18). Bogda significantly increased in the central segment samples after the depositional stage of Xishanyao. Moreover, samples SS001 and ZKD001 significantly differed (8% and 34%) in the proportion of Jueluotag in the Late Jurassic, indicating that Jueluotag was no longer a source for the western part of the basin in the Late Jurassic (Figure 18e–g). Source decomposition showed that the proportion of Bogda sources increased overall (Figure 15), implying that the western segment of Bogda experienced an uplift before the Middle Jurassic (Figure 18b), which is consistent with the cooling ages of previous low-temperature thermochronology (Figure 3).

However, in the north-central and northeastern sides of the Turpan-Hami basin, the heavy minerals were dominated by stable heavy minerals, such as zircon, garnet, and oxides of titanium, with minor unstable minerals [31]. Moreover, in the Sanjianfang depositional stage, large-scale alluvial fans were distributed along the northern margin of the Turpan-Hami basin, and the heavy-mineral results showed a significant increase in magnetite mineral content in the eastern part, with stable minerals still predominating in the central region (Figure 18c,d) [31]. Song et al. [107] found tectonic deformation and large amounts of marine-chlorite unstable heavy minerals during the Middle–Late Jurassic Toutunhe depositional stage based on seismic profiling and heavy-mineral analyses. Moreover, the abundance of unstable heavy minerals at the piedmont of Bogda and at the northern margin of the Turpan-Hami basin all suggest that the uplift of Bogda was intense, especially for the central section of Bogda (Figure 18e,f) [31,38]; this demonstration shows the distinctive differential segmental uplift nature of Bogda (Figure 18).

In addition, various lines of investigation, including evidence from (1) thermochronology studies on the Mesozoic and Cenozoic strata in the NW China basin and surrounding regions [92–109] (Figure 3); (2) a volcano geochemistry study on Mesozoic strata in Bogda [69]; (3) heavy-mineral research in the Turpan-Hami basin [31,38]; (4) climate, stratigraphy, and provenance analyses [23,28,32–35,42,55,91] and sediments preserved in the NW China basin [105,108]; and (5) paleocurrents and tectonic deformation [32,109,110], suggested that Tien Shan was also highly active during the Mesozoic, and especially, Bogda was the most remarkable. The western and eastern segments of Bogda successively experienced a rapid uplift after the Early Jurassic. After the uplift of the central segment of Bogda in the Toutunhe depositional stage, Bogda began to experience an uplift on a large scale. (Figure 18a–f). Central Tien Shan and Jueluotag tended to resurrect during the Cretaceous, somewhat inaugurating the Cenozoic tectonic activity (Figure 18g). Previous studies showed that apatite fission tracks in the northern piedmont of Bogda are younger, mainly younger than 60 Ma (Figure 3). Meanwhile, the younger ages (11 ± 1 Ma; 16 ± 2 Ma; 24 ± 4 Ma) of the Fukang area to the northeast mainly reflect the later uplift phase in the Oligocene–Miocene [100] (Figure 3); there is no doubt that this study further supports our conclusions.

Meanwhile, central Tien Shan and Jueluotag gradually stabilized before the Cretaceous. A comparison with samples deposited at Xishanyao in the western segment of northern Tien Shan revealed that the most striking feature was the predominance of samples of Carboniferous–Permian ages and Jurassic ages from the Toutunhe–Qigu Formations in the western segment of northern Tien Shan (Figures 8 and 10), which indicated that the Bogda uplift was intense after the late development of Xishanyao, that volcanism was intense in the vicinity of northern Tien Shan, that Tien Shan ended quasi-planification, and that provenance could be then ascribed to northern Tien Shan, with volcanic debris being found in the southern part of the Junggar basin (Figure 18e) [23]. The Triassic- and Cretaceous-age zircons produced by samples from the western segment of northern Tien Shan were mainly due to the recycling of older strata. In contrast, the provenance of the samples from the eastern part of the Turpan-Hami basin was primarily ascribable to the Harlik belt, where Triassic granites are widespread. Samples from the western part of northern Tien Shan had Jurassic detrital zircons, mainly attributable to the intense and prolonged volcanic activity on the southern margin of the Junggar basin, which deposited massive tuffs. The predominantly Carboniferous–Permian age scale suggests a new phase of intense uplift in northern Tien Shan and Bogda (Figure 18g).

5.2. A preliminary Exploration of the Limitations of Inverse Monte Carlo Model Decomposition of Detrital-Zircon Provenance

The sample-provenance decomposition was carried out using the inverse Monte Carlo method, as shown in Figures 14–17. The overall situation was relatively well simulated, but there were still a few samples that did not fit well or had similar decomposition results in the source areas, especially the samples that were widely geographically separated from the source areas (Figure 14; Hao-03; SXG-06; JJS12; JJS13; TS12-86). The average percentage of Jueluotag sources in the samples of the Early Jurassic reached 51.8%. Samples JJS54, WGL-03, JDW6, XJ10-015, and XJ10-016 accounted for more than 24% of the Jueluotag sources, with JDW6 accounting for nearly 43% (Figures 14 and 15). However, during the early Badaowan and the Sangonghe depositional stages, the lake pool in the Turpan-Hami basin was widely distributed [34]. Thus, in this period, provenance ascribable to Jueluotag could not be transported to the Bogda piedmont region (Figure 18a). Therefore, Bogda did not experience any uplift, only as positive topography, the provenance of its adjacent areas being ascribable to it (Figure 18a). The north-central parts of the Turpan-Hami basin may have derived from the Qitai paleo-uplift region [42].

In terms of the technical method, due to a certain degree of error in the inverse Monte Carlo mixed model, the detrital-zircon populations were not sufficient. Regarding the source area, the age spectra of the source areas were quite similar and not easily distinguishable or the source-area assignments of the two samples were genuinely similar (Figure 15; JDW-3-6). In addition, it was also probably influenced by the recycling of sedimentary rocks from older strata. The reactivation of Early Mesozoic magmatism in central Tien Shan [103] and the recycled Triassic clastic sediments in the late Middle and Late Jurassic [55,111] brought a great shock to the inverse Monte Carlo model in the dissecting of the source components of detrital zircons. In addition, magmatic activity could also have biased the results. For example, the presence of contemporaneous Jurassic dates indicated the existence of magmatic activity at the southern margin of the Junggar basin in this period, and Yang et al. [22], Fang et al. [23], and Jolivet et al. [55] noted many Jurassic detrital zircons at the southern margin of the Junggar basin. It is also essential to consider that sandstone detrital zircons are inherently hysteretic.

However, most samples fitted relatively successfully. The results of the inverse Monte Carlo mixed model, which dissected provenance components to reconstruct the tectonic evolution of the eastern Tien Shan region, are consistent with those reported in previous work (Figure 18). The more compatible the mixed provenance was, the closer the fitted line was to the cumulative-probability curves for the three provenances (Figures 14–17). Further work needs to be conducted on reducing and avoiding these potential errors.

6. Conclusions

Detrital-zircons U-Pb age data from Late Mesozoic sandstone in the eastern Tien Shan region provided the essential constraints of the provenance transition of the Tupan-Hami basin and the tectonic evolution of Late Mesozoic Bogda and its adjacent areas. The study revealed that the inverse Monte Carlo method for interpreting detrital-zircon provenance has limitations. At the same time, Tien Shan was also highly active during the Mesozoic, and especially, Bogda was the most remarkable. Simultaneously, there was a significant differential segmental exhumation nature. Central Tien Shan and Jueluotag gradually stabilized before the Cretaceous. Details of the presentation are as follows:

1. During the Early Jurassic, Bogda provided few sources, merely as positive topography;
2. From the Early Jurassic to the Cretaceous, the source proportion of Bogda gradually increased over time, especially the large-scale uplift and denudation that occurred after the development of the Qigu Formation;
3. The proportions of the Jueluotag and central Tien Shan gradually declined as a group, stabilizing before the Cretaceous. Central Tien Shan showed a slightly growing trend (41.3%) from the Early Jurassic to the Middle Jurassic and then gradually decreased to 20.3%, still accounting for a sizeable proportion of sources;
4. Similar to central Tien Shan, Jueluotag gradually decreased from an initial 51.8% to 14.9% in the Late Jurassic, but the proportion increased again to 26% in the Cretaceous;
5. Central Tien Shan and Jueluotag tended to resurrect during the Cretaceous, somewhat inaugurating the Cenozoic tectonic activity.

Supplementary Materials: The following supporting information can be downloaded at: <https://www.mdpi.com/article/10.3390/min12080926/s1>, Table S1: LA-ICP-MS zircon U-Pb data of the sandstone; Table S2: Summary of samples statistics; Table S3: Results of decomposition of detrital zircon samples by Monte Carlo model.

Author Contributions: Conceptualization, Y.Q. and C.L.; methodology, Y.Q.; software, Y.Q.; validation, L.Y., X.J. and H.P.; formal analysis, Y.Q.; investigation, L.Y.; resources, C.L.; data curation, L.Y.; writing—original draft preparation, Y.Q.; writing—review and editing, Y.Q.; visualization, L.Y.; supervision, C.L.; project administration, H.P.; funding acquisition, C.L. All authors have read and agreed to the published version of the manuscript.

Funding: National Natural Science Foundation of China (42102128, 42072132, 41972153), the Natural Science Foundation of Shaanxi Province (2021JQ-591, 2018JM4001), and Land and Resources Survey Project of China (DD20189612, 1212010881632).

Institutional Review Board Statement: Not applicable.

Informed Consent Statement: Not applicable.

Data Availability Statement: All data generated or analyzed during this study are included in this published article (and its Supplementary Materials).

Conflicts of Interest: The authors declare no conflict of interest.

References

1. Finch, R.J.; Hancher, J.M. Structure and Chemistry of Zircon and Zircon-Group Minerals. *Rev. Mineral. Geochem.* **2003**, *53*, 1–25. [\[CrossRef\]](#)
2. Gehrels, G.E. Detrital zircon U-Pb geochronology applied to tectonics. *Annu. Rev. Earth Planet. Sci.* **2014**, *42*, 127–149. [\[CrossRef\]](#)
3. Gehrels, G.E.; Blakey, R.; Karlstrom, K.E.; Timmons, J.M.; Dickinson, B.; Pecha, M. Detrital zircon U-Pb geochronology of Paleozoic strata in the Grand Canyon, Arizona. *Lithosphere* **2011**, *3*, 183–200. [\[CrossRef\]](#)
4. Thomas, W.A. Detrital-zircon geochronology and sedimentary provenance. *Lithosphere* **2011**, *3*, 304–308. [\[CrossRef\]](#)
5. Siégl, C.; Bryan, S.E.; Allen, C.M.; Gust, D.A. Use and abuse of zircon-based thermometers: A critical review and a recommended approach to identify antecrystic zircons-ScienceDirect. *Earth-Sci. Rev.* **2018**, *176*, 87–116. [\[CrossRef\]](#)
6. Vermeesch, P. Multi-sample comparison of detrital age distributions. *Chem. Geol.* **2013**, *341*, 140–146. [\[CrossRef\]](#)
7. Saylor, J.E.; Sundell, K.E. Quantifying comparison of large detrital geochronology data sets. *Geosphere* **2016**, *12*, 203–220. [\[CrossRef\]](#)
8. Sundell, K.E.; Saylor, J.E. Unmixing detrital geochronology age distributions. *Geochim. Geophys. Geosystems* **2017**, *18*, 2872–2886. [\[CrossRef\]](#)

9. Satkoski, A.M.; Wilkinson, B.H.; Hieptas, J.; Samson, S.D. Likeness among detrital zircon populations—An approach to the comparison of age frequency data in time and space. *GSA Bull.* **2013**, *125*, 1783–1799. [\[CrossRef\]](#)
10. Mao, J.W.; Goldfarb, R.J.; Wang, Y.T.; Hart, C.J.; Wang, Z.L.; Yang, J.M. Late Paleozoic base and precious metal deposits, East Tianshan, Xinjiang, China: Characteristics and geodynamic setting. *Episodes* **2005**, *28*, 23–36. [\[CrossRef\]](#)
11. Sengör, A.M.C.; Natal'in, B.A.; Burtman, V.S. Evolution of the Altaid tectonic collage and Paleozoic crustal growth in Eurasia. *Nature* **1993**, *364*, 299–307. [\[CrossRef\]](#)
12. Windley, B.F.; Alexeiev, D.; Xiao, W.J.; Kröner, A.; Badarch, G. Tectonic models for accretion of the Central Asian Orogenic Belt. *J. Geol. Soc.* **2007**, *164*, 31–47. [\[CrossRef\]](#)
13. Xiao, W.J.; Windley, B.F.; Hao, J.; Zhai, M.G. Accretion leading to collision and the Permian Solonker suture, Inner, Mongolia, China: Termination of the Central Asian Orogenic Belt. *Tectonics* **2003**, *22*, 1069. [\[CrossRef\]](#)
14. Xiao, W.J.; Windley, B.F.; Yan, Q.R.; Qin, K.Z.; Chen, H.L.; Yuan, C.; Sun, S. SHRIMP zircon age of the Aermantai ophiolite in the North Xinjiang, China, and its tectonic implications. *Acta Geol. Sin.* **2006**, *80*, 32–36. (In Chinese with English abstract).
15. Xiao, W.J.; Huang, B.C.; Han, C.M.; Sun, S.; Li, J.L. A review of the western part of the Altaids: A key to understanding the architecture of accretionary orogens. *Gondwana Res.* **2010**, *18*, 253–273. [\[CrossRef\]](#)
16. Allen, M.B.; Windley, B.F.; Zhang, C. Palaeozoic collisional tectonics and magmatism of the Chinese Tien Shan, central Asia. *Tectonophysics* **1993**, *220*, 89–115. [\[CrossRef\]](#)
17. Carroll, A.R.; Graham, S.A.; Hendrix, M.S.; Ying, D.; Zhou, D. Late Paleozoic tectonic amalgamation of northwestern China: Sedimentary record of the northern Tarim, northwestern Turpan, and southern Junggar basins. *GSA Bull.* **1995**, *107*, 571–594. [\[CrossRef\]](#)
18. Gao, J.; Long, L.L.; Klemd, R.; Qian, Q.; Liu, D.Y.; Xiong, X.M.; Yang, F.Q. Tectonic evolution of the South Tianshan orogen and adjacent regions, NW China: Geochemical and age constraints of granitoid rocks. *Int. J. Earth Sci.* **2009**, *98*, 1221–1238. [\[CrossRef\]](#)
19. Xiao, W.; Windley, B.F.; Allen, M.B.; Han, C. Paleozoic multiple accretionary and collisional tectonics of the Chinese Tianshan orogenic collage. *Gondwana Res.* **2013**, *23*, 1316–1341. [\[CrossRef\]](#)
20. Charreau, J.; Chen, Y.; Gilder, S.; Dominguez, S.; Avouac, J.P.; Sen, S.; Wang, W.M. Magnetostratigraphy and rock magnetism of the Neogene Kuitun He section (northwest China): Implications for Late Cenozoic uplift of the Tianshan Mountains. *Earth Planet. Sci. Lett.* **2005**, *230*, 177–192. [\[CrossRef\]](#)
21. Charreau, J.; Gilder, S.; Chen, Y.; Dominguez, S.; Avouac, J.P.; Sen, S.; Wang, W.M. Magnetostratigraphy of the Yaha section, Tarim Basin (China): 11 Ma acceleration in erosion and uplift of the Tian Shan mountains. *Geology* **2006**, *34*, 181–184. [\[CrossRef\]](#)
22. Jolivet, M.; Dominguez, S.; Charreau, J.; Chen, Y.; Li, Y.A.; Wang, Q.C. Mesozoic and Cenozoic tectonic history of the Central Chinese Tian Shan: Reactivated tectonic structures and active deformation. *Tectonics* **2010**, *29*, TC6019. [\[CrossRef\]](#)
23. Fang, Y.N.; Wu, C.D.; Guo, Z.J.; Hou, K.J.; Dong, L.; Wang, L.X.; Li, L.L. Provenance of the southern Junggar Basin in the Jurassic: Evidence from detrital zircon geochronology and depositional environments. *Sediment. Geol.* **2015**, *315*, 47–63. [\[CrossRef\]](#)
24. Fang, Y.N.; Wu, C.D.; Wang, Y.Z.; Hou, K.J.; Gao, Z.J. Topographic evolution of the Tianshan Mountains and their relation to the Junggar and Turpan Basins, Central Asia, from the Permian to the Neogene. *Gondwana Res.* **2019**, *75*, 47–67. [\[CrossRef\]](#)
25. Ji, H.J.; Tao, H.; Wang, Q.; Qiu, Z.; Ma, D.; Qiu, J.; Liao, P. Early to Middle Jurassic tectonic evolution of the Bogda Mountains, Northwest China: Evidence from sedimentology and detrital zircon geochronology. *J. Asian Earth Sci.* **2018**, *153*, 57–74. [\[CrossRef\]](#)
26. Ji, H.J.; Tao, H.F.; Qiu, J.L.; Wei, H.Y. Provenance of Middle Jurassic clastic rocks from the Bogda region of Eastern Tianshan and its implications. *Int. Geol. Rev.* **2019**, *6*, 1319–1342. [\[CrossRef\]](#)
27. Zhang, X.R.; Zhao, G.C.; Sun, M.; Han, Y.G.; Liu, Q. Triassic magmatic reactivation in Eastern Tianshan, NW China: Evidence from geochemistry and zircon U-Pb-Hf isotopes of granites. *J. Asian Earth Sci.* **2017**, *145*, 446–459. [\[CrossRef\]](#)
28. Yang, Y.T.; Song, C.C.; He, S. Jurassic tectonostratigraphic evolution of the Junggar basin, NW China: A record of Mesozoic intraplate deformation in Central Asia. *Tectonics* **2015**, *34*, 86–115. [\[CrossRef\]](#)
29. Graham, S.A.; Hendrix, M.S.; Wang, L.B.; Carroll, A.R. Collisional successor basins of western China: Impact of tectonic inheritance on sand composition. *GSA Bull.* **1993**, *105*, 323–344. [\[CrossRef\]](#)
30. Greene, T.J.; Carroll, A.R.; Hendix, M.S.; Graham, S.A.; Wartes, M.A.; Abbink, O.A. Sedimentary record of Mesozoic deformation and inception of the Turpan-Hami basin, north-west China. *GSA Bull.* **2001**, *194*, 317–340. [\[CrossRef\]](#)
31. Guan, Y.Z.; Liu, C.Y.; Zhang, S.H.; Wang, J.Q.; Liang, H. The characteristics of the heavy mineral assemblages of the Middle Jurassic in the north central Tuha Basin and their constraints on the uplift of Bogda Mountain. *Chin. J. Geol.* **2018**, *53*, 1389–1404. (In Chinese with English abstract).
32. Hendrix, M.S.; Graham, S.A.; Carroll, A.R.; Sobel, E.R.; McKnight, C.L.; Schulein, B.J.; Wang, Z. Sedimentary record and climatic implications of recurrent deformation in the Tien Shan: Evidence from Mesozoic strata of the north Tarim, south Junggar, and Turpan basins, northwest China. *GSA Bull.* **1992**, *104*, 53–79. [\[CrossRef\]](#)
33. Ji, H.J.; Tao, H.F.; Wang, Q.; Ma, D.X.; Hao, L.W. Petrography, geochemistry, and geochronology of Lower Jurassic sedimentary rocks from the Northern Tianshan (West Bogda region), Northwest China: Implications for provenance and tectonic evolution. *Geol. J.* **2018**, *54*, 1688–1714. [\[CrossRef\]](#)
34. Shao, L.Y.; Zhang, P.F.; Hilton, J.; Gayer, R.; Wang, Y.B.; Zhao, C.Y.; Luo, Z. Paleoenvironments and paleogeography of the Lower and lower Middle Jurassic coal measures in the Turpan-Hami oil-prone coal basin, northwestern China. *AAPG Bull.* **2003**, *87*, 335–355. [\[CrossRef\]](#)

35. Tang, W.H.; Zhang, Z.C.; Li, J.F.; Li, K. Late Paleozoic to Jurassic tectonic evolution of the Bogda region (northwest China): Evidence from detrital zircon U-Pb geochronology. *Tectonophysics* **2014**, *626*, 144–156. [\[CrossRef\]](#)
36. Zhao, R.; Zhang, J.Y.; Zhou, C.M.; Zhang, Z.J.; Chen, S.; Stockli, D.F.; Wang, H. Tectonic evolution of Tianshan-Bogda-Kelameili mountains, clastic wedge basin infill and chronostratigraphic divisions in the source-to-sink systems of Permian-Jurassic, southern Junggar Basin. *Mar. Petrol. Geol.* **2020**, *114*, 104–200. [\[CrossRef\]](#)
37. Shen, C.B.; Mei, L.F.; Liu, L.; Tang, J.G.; Zhou, F. Evidence from apatite and zircon fission track analysis for Mesozoic-Cenozoic uplift thermal history of Bogda Mountain of Xinjiang, Northwest China. *Mar. Geol. Quatern. Geol.* **2006**, *26*, 87–92. (In Chinese with English abstract).
38. Zhou, T.Q.; Wu, C.D.; Yuan, B.; Shi, Z.K.; Wang, J.L.; Zhu, W.; Ma, J. Characteristics of Jurassic heavy minerals in the southern margin of Junggar Basin and their provenance indicating significance. *Pet. Explor. Dev.* **2019**, *46*, 65–78. (In Chinese with English abstract). [\[CrossRef\]](#)
39. Chen, K.; Lin, W.; Wang, Q.C. The Bogeda Shan uplifting: Evidence from multiple phases of deformation. *Asian Earth Sci.* **2015**, *99*, 1–12. [\[CrossRef\]](#)
40. Fang, S.H.; Guo, Z.J.; Song, Y.; Wu, C.D.; Zhang, Z.C.; Wang, M.N.; Fan, R.D. Sedimentary facies evolution and basin pattern of the Jurassic in southern margin region of Junggar Basin. *J. Palaeogeogr.* **2005**, *7*, 347–356. (In Chinese with English abstract).
41. Li, W.; Hu, J.M.; Li, D.P.; Liu, J.X.; Sun, Y.P.; Liang, J.W. Analysis of the Late Paleozoic and Mesozoic paleocurrents and its constructional significance of the northern Bogdashan, Xinjiang. *Acta Sediment. Sin.* **2007**, *25*, 283–292. (In Chinese with English abstract).
42. Shao, L.; Stattegger, K.; Li, W.H.; Haupt, B.J. Depositional style and subsidence history of the Turpan Basin (NW China). *Sediment. Geol.* **1999**, *128*, 155–169. [\[CrossRef\]](#)
43. Shen, T.Y.; Chen, Y.; Wang, G.C.; Ji, J.L.; Wang, Y.; Zhang, P.; Xu, Z.Z. Detrital zircon geochronology analysis of the Late Mesozoic deposition in the Turpan-Hami basin: Implications for the uplift history of the Eastern Tien Shan, northwestern China. *Terra Nova* **2019**, *32*, 166–178. [\[CrossRef\]](#)
44. Zhang, C.H.; Zhang, D.B.; Liu, C.L.; Zhang, Z.Q.; Wang, Q.X.; Yu, Q.X. Stratigraphic constraints on the initial uplift age of Bogda Shan, Xinjiang, northwest China. *Earth Sci. Front.* **2005**, *12*, 294–302. (In Chinese with English abstract).
45. Xiao, W.J.; Sun, M.; Santosh, M. Continental reconstruction and metallogeny of the Circum-Junggar regions and termination of the southern Central Asian Orogenic Belt. *Geosci. Front.* **2015**, *6*, 137–140. [\[CrossRef\]](#)
46. Yakubchuk, A. Architecture and mineral deposit settings of the Altaid orogenic collage: A revised model. *J. Asian Earth Sci.* **2004**, *23*, 761–779. [\[CrossRef\]](#)
47. Buslov, M.M.; Watanabe, T.; Fujiwara, Y.; Iwata, K.; Smirnova, L.V.; Safonova, I.Y.; Kiryanova, A.P. Late Paleozoic faults of the Altai region, Central Asia: Tectonic pattern and model of formation. *J. Asian Earth Sci.* **2004**, *23*, 655–671. [\[CrossRef\]](#)
48. Coleman, R.G. Continental growth of northwest China. *Tectonics* **1989**, *8*, 621–635. [\[CrossRef\]](#)
49. Han, B.F.; He, G.Q.; Wang, X.C.; Guo, Z.J. Late Carboniferous collision between the Tarim and Kazakhstan-Yili terranes in the western segment of the South Tien Shan Orogen, Central Asia, and implications for the Northern Xinjiang, western China. *Earth-Sci. Rev.* **2011**, *109*, 74–93. [\[CrossRef\]](#)
50. Huang, H.; Zhang, Z.C.; Santosh, M.; Zhang, D.Y.; Wang, T. Petrogenesis of the Early Permian volcanic rocks in the Chinese South Tianshan: Implications for crustal growth in the Central Asian Orogenic Belt. *Lithos* **2015**, *228–229*, 23–42. [\[CrossRef\]](#)
51. Kröner, A.; Kovach, V.; Belousova, E.; Hegner, E.; Armstrong, R.; Dolgoplova, A.; Rytisk, E. Reassessment of continental growth during the accretionary history of the Central Asian Orogenic Belt. *Gondwana Res.* **2014**, *25*, 103–125. [\[CrossRef\]](#)
52. Xiao, W.J.; Windley, B.F.; Huang, B.C.; Han, C.M.; Yuan, C.; Chen, H.L.; Li, J.L. End-Permian to mid-Triassic termination of the accretionary processes of the southern Altaids: Implications for the geodynamic evolution, Phanerozoic continental growth, and metallogeny of Central Asia. *Int. J. Earth Sci.* **2009**, *98*, 1189–1217. [\[CrossRef\]](#)
53. Xiao, W.J.; Windley, B.F.; Yuan, C.; Sun, M.; Han, C.M.; Lin, S.F.; Sun, S. Paleozoic multiple subduction-accretion processes of the southern Altaids. *Am. J. Sci.* **2009**, *309*, 221–270. [\[CrossRef\]](#)
54. Xiao, W.J.; Zhang, L.C.; Qin, K.Z.; Sun, S.; Li, J.L. Paleozoic accretionary and collisional tectonics of the Eastern Tianshan (China): Implications for the continental growth of central Asia. *Am. J. Sci.* **2004**, *304*, 370–395. [\[CrossRef\]](#)
55. Jolivet, M.; Bourquin, S.; Heilbronn, G.; Robin, C.; Barrier, L.; Dabard, M.P.; Fu, B. The Upper Jurassic-Lower Cretaceous alluvial fan deposits of the Kalaza Formation (Central Asia): Tectonic pulse or increased aridity? *GSA Bull.* **2016**, *427*, 491–521. [\[CrossRef\]](#)
56. Avouac, J.P.; Tapponnier, P.; Bai, M.; You, H.; Wang, G. Active thrusting and folding along the northern Tien Shan and late Cenozoic rotation of the Tarim relative to Dzungaria and Kazakhstan. *J. Geophys. Res. Solid Earth* **1993**, *98*, 6755–6804. [\[CrossRef\]](#)
57. Hendrix, M.S.; Dumitru, T.A.; Graham, S.A. Late Oligocene-early Miocene unroofing in the Chinese Tian Shan: An early effect of the India-Asia collision. *Geology* **1994**, *22*, 487–490. [\[CrossRef\]](#)
58. Yang, W.; Jolivet, M.; Dupont-Nivet, G.; Guo, Z.J. Mesozoic-Cenozoic tectonic evolution of southwestern Tian Shan: Evidence from detrital zircon U/Pb and apatite fission track ages of the Ulugqat area, Northwest China. *Gondwana Res.* **2014**, *26*, 986–1008. [\[CrossRef\]](#)
59. Han, Y.G.; Zhao, G.C. Final amalgamation of the Tianshan and Junggar orogenic collage in the southwestern Central Asian Orogenic Belt: Constraints on the closure of the Paleo-Asian Ocean. *Earth Sci. Rev.* **2018**, *186*, 129–152. [\[CrossRef\]](#)
60. Xia, L.Q.; Xu, X.Y.; Xia, Z.C.; Li, X.M.; Ma, Z.P.; Wang, L.S. Petrogenesis of Carboniferous rift-related volcanic rocks in the Tianshan, northwestern China. *GSA Bull.* **2004**, *116*, 419–433. [\[CrossRef\]](#)

61. Xia, L.Q.; Xia, Z.C.; Xu, X.Y.; Li, X.M.; Ma, Z.P. Relative contributions of crust and mantle to the generation of the Tianshan Carboniferous rift-related basic lavas, northwestern China. *J. Asian Earth Sci.* **2008**, *31*, 357–378. [\[CrossRef\]](#)
62. Xie, W.; Xu, Y.G.; Luo, Z.Y.; Liu, H.Q.; Hong, L.B.; Ma, L. Petrogenesis and geodynamic implications of the Late Carboniferous felsic volcanics in the Bogda belt, Chinese Northern Tianshan. *Gondwana Res.* **2016**, *39*, 165–179. [\[CrossRef\]](#)
63. Yang, W.; Jolivet, M.; Dupont-Nivet, G.; Guo, Z.J.; Zhang, Z.C.; Wu, C.D. Source to sink relations between the Tien Shan and Junggar Basin (northwest China) from Late Palaeozoic to Quaternary: Evidence from detrital U-Pb zircon geochronology. *Basin Res.* **2013**, *25*, 219–240. [\[CrossRef\]](#)
64. Wali, G.; Wang, B.; Cluzel, D.; Zhong, L. Carboniferous-Early Permian magmatic evolution of the Bogda Range (Xinjiang, NW China): Implications for the Late Paleozoic accretionary tectonics of the SW Central Asian Orogenic Belt. *J. Asian Earth Sci.* **2018**, *153*, 238–251. [\[CrossRef\]](#)
65. Zhang, X.R.; Zhao, G.C.; Sun, M.; Eizenhöfer, P.R.; Han, Y.G.; Hou, W.Z.; Xu, B. Tectonic evolution from subduction to arc-continent collision of the Junggar ocean: Constraints from U-Pb dating and Hf isotopes of detrital zircons from the North Tien shan belt, NW China. *GSA Bull.* **2017**, *128*, 644–660. [\[CrossRef\]](#)
66. Zhao, L.D.; Chen, H.Y.; Zhang, L.; Zhang, W.F.; Yang, J.T.; Yan, X. The Late Paleozoic magmatic evolution of the Aqishan-Yamansu belt, Eastern Tianshan: Constraints from geochronology, geochemistry and Sr-Nd-Pb-Hf isotopes of igneous rocks. *J. Asian Earth Sci.* **2018**, *153*, 170–192. [\[CrossRef\]](#)
67. Shu, L.S.; Charvet, J.; Guo, L.Z.; Lu, H.F.; Laurent-Charvet, S. A large-scale Palaeozoic dextral ductile strike-slip zone: The Aqqikkudug-Weiya zone along the northern margin of the Central Tianshan Belt, Xinjiang, NW China. *Acta Geo. Sin.* **1999**, *73*, 148–162. [\[CrossRef\]](#)
68. Wang, B.; Cluzel, D.; Jahn, B.M.; Shu, L.; Chen, Y.; Zhai, Y.; Sizaret, S. Late Paleozoic pre-and syn-kinematic plutons of the Kangguer-Huangshan shear zone: Inference on the tectonic evolution of the eastern Chinese north Tianshan. *Am. J. Sci.* **2014**, *314*, 43–79. [\[CrossRef\]](#)
69. Liu, H.Q.; Xu, Y.G.; Wei, G.J.; Wei, J.X.; Yang, F.; Chen, X.Y.; Wei, X. B isotopes of Carboniferous-Permian volcanic rocks in the Tuha basin mirror a transition from subduction to intraplate setting in Central Asian Orogenic Belt. *J. Geophys. Res. Sol. Ea.* **2016**, *121*, 7946–7964. [\[CrossRef\]](#)
70. Ma, X.H.; Chen, B.; Wang, C.; Yan, X.L. Early Paleozoic subduction of the Paleo-Asian Ocean: Zircon U-Pb geochronological, geochemical and Sr-Nd isotopic evidence from the Harlik pluton, Xinjiang. *Acta Petrol. Sin.* **2015**, *31*, 89–104. (In Chinese with English abstract).
71. Yuan, C.; Sun, M.; Wilde, S.; Xiao, W.J.; Xu, Y.G.; Long, X.P.; Zhao, G.C. Post-collisional plutons in the Balikun region, East Chinese Tianshan: Evolving magmatism in response to extension and slab break-off. *Lithos* **2010**, *119*, 269–288. [\[CrossRef\]](#)
72. Ma, J. Study on the Huangcaopo Group in the Eastern Junggar. *J. Mineral. Petrol.* **1999**, *19*, 5–55. (In Chinese with English abstract).
73. Chen, X.J.; Shu, L.S.; Santosh, M.; Zhao, X.X. Island arc-type bimodal magmatism in the eastern Tianshan Belt, Northwest China: Geochemistry, zircon U-Pb geochronology and implications for the Paleozoic crustal evolution in Central Asia. *Lithos* **2013**, *168–169*, 48–66. [\[CrossRef\]](#)
74. Huang, B.; Fu, D.; Kusky, T.; Ruan, K.P.; Zhou, W.X.; Zhang, X.H. Sedimentary provenance in response to Carboniferous arc-basin evolution of East Junggar and North Tianshan belts in the southwestern Central Asian Orogenic Belt. *Tectonophysics* **2018**, *722*, 324–341. [\[CrossRef\]](#)
75. Hu, A.; Jahn, B.M.; Zhang, G.; Chen, Y.; Zhang, Q. Crustal evolution and Phanerozoic crustal growth in northern Xinjiang: Nd isotopic evidence. Part I. Isotopic characterization of basement rocks. *Tectonophysics* **2000**, *328*, 15–51. [\[CrossRef\]](#)
76. Huang, Z.; Long, X.; Kröner, A.; Yuan, C.; Wang, Y.; Chen, B.; Zhang, Y. Neoproterozoic granitic gneisses in the Chinese Central Tianshan Block: Implications for tectonic affinity and Precambrian crustal evolution. *Precambrian Res.* **2015**, *269*, 73–89. [\[CrossRef\]](#)
77. Wang, X.S.; Gao, J.; Klemd, R.; Jiang, T.; Li, J.L.; Zhang, X.; Xue, S.C. The Central Tianshan Block: A microcontinent with a Neoproterozoic-Paleoproterozoic basement in the southwestern Central Asian Orogenic Belt. *Precambrian Res.* **2017**, *295*, 130–150. [\[CrossRef\]](#)
78. Ma, X.; Shu, L.; Meert, J.G.; Li, J. The Paleozoic evolution of Central Tianshan: Geochemical and geochronological evidence. *Gondwana Res.* **2014**, *25*, 797–819. [\[CrossRef\]](#)
79. Gao, J.; Klemd, R. Formation of HP-LT rocks and their tectonic implications in the western Tianshan Orogen, NW China: Geochemical and age constraints. *Lithos* **2003**, *66*, 1–22. [\[CrossRef\]](#)
80. Allen, M.B.; Şengör, A.M.C.; Natalin, B.A. Junggar, Turfan and Alakol basins as Late Permian to? Early Triassic extensional structures in a sinistral shear zone in the Altaid orogenic collage, Central Asia. *J. Geol. Soc.* **1995**, *152*, 327–338. [\[CrossRef\]](#)
81. Gao, G.; Yang, S.R.; Liang, H.; Wang, Z.Y.; Li, X.N. The origin and secondary alteration of dissolved gas in oil: A case study from the western Tu-Ha Basin, China. *J. Nat. Gas Sci. Eng.* **2018**, *52*, 283–294. [\[CrossRef\]](#)
82. Han, S.B.; Zhang, J.C.; Zhou, Y.Q.; Bai, S.T.; Huang, L.X.; Wang, C.S.; Huang, W.D. Formation and accumulation of lower Jurassic tight gas sands field in Kekeya region of Tuha Basin, northwestern China. *J. Nat. Gas Sci. Eng.* **2016**, *29*, 101–109. [\[CrossRef\]](#)
83. Li, W.H.; Zhou, L.F.; Liu, Y.Q.; Liang, S.J.; Long, D.J. Evolution of sedimentary framework and environment of Turpan-Hami basin. *Xinjiang Petrol. Geol.* **1997**, *18*, 135–141. (In Chinese with English abstract).
84. Gu, L.X.; Hu, S.X.; Yu, C.S.; Li, H.Y.; Xiao, X.J.; Yan, Z.F. Carboniferous volcanites in the Bogda orogenic belt of eastern Tianshan: Their tectonic implications. *Acta Petrol. Sin.* **2000**, *16*, 305–316. (In Chinese with English abstract).

85. Kuang, L.C.; Zhang, Y.Q.; Zha, M.; Chen, Z.H.; Kong, Y.H.; Zhang, Y. Carboniferous tectonic setting and evolution in northern Xinjiang, China. *Acta Geol. Sin.* **2013**, *87*, 311–320. (In Chinese with English abstract).
86. Allen, M.B.; Windley, B.F.; Zhang, C.; Zhao, Z.Y.; Wang, G.R. Basin evolution within and adjacent to the Tien Shan Range, NW China. *J. Geol. Soc.* **1991**, *148*, 369–378. [\[CrossRef\]](#)
87. Shu, L.S.; Wang, B.; Zhu, W.B.; Guo, Z.J.; Charvet, J.; Zhang, Y. Timing of initiation of extension in the Tianshan, based on structural, geochemical and geochronological analyses of bimodal volcanism and olistostrome in the Bogda Shan (NW China). *Int. J. Earth Sci.* **2011**, *100*, 1647–1663. [\[CrossRef\]](#)
88. Greene, T.J.; Carroll, A.R.; Wartes, M.; Graham, S.A.; Wooden, J.L. Integrated provenance analysis of a complex orogenic terrane: Mesozoic uplift of the Bogda Shan and inception of the Turpan-Hami Basin, NW China. *J. Sediment. Res.* **2005**, *75*, 251–267. [\[CrossRef\]](#)
89. Li, D. Hydrocarbon occurrences in the petroliferous basins of western China. *Mar. Petrol. Geol.* **1995**, *12*, 26–34. [\[CrossRef\]](#)
90. Wu, T.; Zhao, W. *Formation and Distribution of Oil and Gas Fields in Turpan-Hami Coal-Bearing Basin*; Petroleum Industry Press: Beijing, China, 1997; pp. 21–25. (In Chinese with English abstract).
91. Li, W.H.; Zhou, L.F.; Liu, Y.Q.; Liang, D.J. Sedimentary pattern and evolution of sedimentary environment in Turpan-Hami Basin. *Xinjiang Pet. Geol.* **1997**, *2*, 135–141. (In Chinese with English abstract).
92. Li, Z.; Peng, S.T. Detrital zircon geochronology and its provenance implications: Responses to Jurassic through Neogene basin-range interactions along northern margin of the Tarim Basin Northwest China. *Basin Res.* **2010**, *22*, 126–138. [\[CrossRef\]](#)
93. Wang, X.W.; Wang, X.W.; Ma, Y.S. Differential exhumation history of Bogda Mountain, Xinjiang, Northwestern China since the Late Mesozoic. *Acta Geol. Sin.* **2007**, *81*, 1507–1517. [\[CrossRef\]](#)
94. Wang, Z.X.; Li, T.; Zhang, J.; Liu, Y.Q.; Ma, Z.J. The uplifting process of the Bogda Mountain during the Cenozoic and its tectonic implication. *Sci. China Earth Sci.* **2008**, *51*, 579–593. [\[CrossRef\]](#)
95. Zhu, W.; Shu, L.; Wan, J.; Sun, Y.; Wang, F.; Zhao, Z. Fission-track evidence for the exhumation history of Bogda-Harlik Mountains Xinjiang, since the Cretaceous. *Acta Geol. Sin.* **2006**, *80*, 16–22. [\[CrossRef\]](#)
96. Shen, C.B.; Mei, L.F.S.; Zhang, W.; Liu, L.; Tang, J.G.; Zhou, F.; Luo, J.C. Fission-track dating evidence on space-time difference of Mesozoic-Cenozoic uplift of the Yilianhabierga Mountain and Bogeda Mountain. *J. Mineral. Petrol.* **2008**, *28*, 63–70. (In Chinese with English abstract).
97. Dumitru, T.A.; Zhou, D.; Chang, E.Z.; Graham, S.A. Uplift, exhumation, and deformation in the Chinese Tien Shan, in Paleozoic and Mesozoic Tectonic Evolution of Central and Eastern Asia—From Continental Assembly to Intracontinental Deformation. *GSA Bull.* **2001**, *194*, 71–99. [\[CrossRef\]](#)
98. Guo, Z.J.; Zhang, Z.C.; Wu, C.D.; Fang, S.H.; Zhang, R. The Mesozoic and Cenozoic exhumation history of Tianshan and comparative studies to the Junggar and Altai Mountains. *Acta Geol. Sin.* **2006**, *80*, 1–15. (In Chinese with English abstract).
99. Yuan, W.M.; Zheng, Q.G.; Bao, Z.K.; Dong, J.Q.; Carter, A.; An, Y.C.; Deng, J. Zircon fission track thermochronology constraints on mineralization epochs in Altai Mountains, northern Xinjiang China. *Radiat. Meas.* **2009**, *44*, 950–954. [\[CrossRef\]](#)
100. Tang, W.H.; Zhang, Z.C.; Li, J.F.; Li, K.; Luo, Z.W.; Chen, Y. Mesozoic and Cenozoic uplift and exhumation of the Bogda Mountain, NW China: Evidence from apatite fission track analysis. *Geosci. Front.* **2015**, *6*, 617–625. [\[CrossRef\]](#)
101. Chen, Y.; Wang, G.C.; Kapp, P.; Shen, T.Y.; Zhang, P.; Zhu, C.Y.; Cao, K. Episodic exhumation and related tectonic controlling during Mesozoic in the Eastern Tien Shan, Xinjiang, northwestern China. *Tectonophysics* **2020**, *796*, 228647. [\[CrossRef\]](#)
102. Gehrels, G.E. Introduction to detrital zircon studies of Paleozoic and Triassic strata in western Nevada and northern California. *GSA Bull.* **2000**, *347*, 1–17. [\[CrossRef\]](#)
103. Zhang, Y.Y.; Yuan, C.; Long, X.P.; Sun, M.; Huang, Z.Y.; Du, L.; Wang, X.Y. Carboniferous bimodal volcanic rocks in the Eastern Tianshan, NW China: Evidence for arc rifting. *Gondwana Res.* **2017**, *43*, 92–106. [\[CrossRef\]](#)
104. Allen, M.B.; Aslop, G.I.; Zhemchuzhnikov, V.G. Dome and basin refolding and transpressive inversion along the Karatau fault system, southern Kazakhstan. *J. Geol. Soc.* **2001**, *158*, 83–95. [\[CrossRef\]](#)
105. Li, Z.; Song, W.J.; Peng, S.T.; Wang, D.X.; Zhang, Z.P. Mesozoic-Cenozoic tectonic relationships between the Kuqa subbasin and Tien Shan, northwest China: Constraints from depositional records. *Sediment. Geol.* **2004**, *172*, 223–249. [\[CrossRef\]](#)
106. Grave, J.D.; Buslov, M.M.; Haute, P.V.D. Distant effects of India-Eurasia convergence and Mesozoic intracontinental deformation in Central Asia: Constraints from apatite fission-track thermochronology. *J. Asian Earth Sci.* **2007**, *29*, 188–204. [\[CrossRef\]](#)
107. Song, Y.; Chen, S.; Zhang, Y.L.; Liang, X.X.; Liang, Y.Y.; Hou, W. Calibration of the Middle and Late Jurassic Basin-Mountain Differentiation Time Limit in Bogda Region, Southeastern Margin of Junggar Basin. *Sci. Technol. Eng.* **2020**, *20*, 924–934. (In Chinese with English abstract).
108. Li, Z.; Tang, W.X.; Peng, S.T.; Xu, J.Q. Detrital zircon U-Pb geochronological and depositional records of the Mesozoic-Cenozoic profile in the southern Junggar Basin, northwest China, and their responses to basin-range tectonic evolution. *Chin. J. Geol.* **2012**, *47*, 1016–1040. (In Chinese with English abstract).
109. Ritts, B.D.; Biffi, U. Mesozoic Northeast Qaidam basin: Response to contractional reactivation of Qilian Shan, and implications for extent of Mesozoic intracontinental deformation in central Asia, in Paleozoic and Mesozoic Tectonic Evolution of Central and Eastern Asia—From Continental Assembly to Intracontinental Deformation. *GSA Bull.* **2001**, *194*, 293–316. [\[CrossRef\]](#)

-
110. Carroll, A.R.; Graham, S.A.; Smith, M.E. Walled sedimentary basins of China. *Basin Res.* **2010**, *22*, 17–32. [[CrossRef](#)]
 111. Liu, D.D.; Zhang, C.; Yao, E.D.; Song, Y.; Jiang, Z.X.; Luo, Q. What generated the Late Permian to Triassic unconformities in the southern Junggar Basin and western Turpan Basin; tectonic uplift, or increasing aridity? *Palaeogeogr. Palaeoclimatol.* **2017**, *468*, 1–17. [[CrossRef](#)]